Supporting Information

Generating zeolite crystals with mesoscopic aperiodic structure to promote catalytic hydroisomerization

Guanyu Qie,‡[a] Quanzheng Deng,‡[b] Donghao Deng,‡[c] Miao Zhai, §[a] Hongxin Ding,[d] Wei Liu,*[c] Lu Han*[b] and Kake Zhu*[a]

[a]State Key Laboratory of Chemical Engineering, School of Chemical Engineering, East China University of Science and Technology, Shanghai 200237, China

[b]School of Chemical Science and Engineering, Tongji University, Shanghai 200092, China

[c]Shanghai Research Institute of Petrochemical Technology, SINOPEC, Shanghai 201208, China

[d]Department of Chemistry, Fudan University, Shanghai 200433, China

‡These authors equally contribute to this work.
*To whom correspondence should be addressed: liuw.sshy@sinopec.com, luhan@tongji.edu.cn or kakezhu@ecust.edu.cn.
§Present Address: Department of Food and Biochemical Engineering, Yantai, Vocational College, Yantai, 264670, China

Table of Contents

1. Experimental

1.1 Chemicals and reagents

1,7-Dibromoheptane ($C_7H_{14}Br_2$, 98%, Shanghai Titan Scientific Co. Ltd.), N,N,N',N'-Tetramethyl-1,6-hexanediamine ($C_{10}H_{24}N_2$, > 99%, Shanghai Macklin Biochemical Reagent Co. Ltd.), methanol (MeOH, 99.9%, super dry, water ≤ 30 ppm, J&K Seal), trimethylamine (TMA, 30 wt. % in ethanol, Shanghai Titan Scientific Co. Ltd.), 1,5-dibromopentane (DBP, 98%, TCI Development Co. Ltd.), sodium hydroxide (NaOH, 96%, Shanghai Titan Scientific Co. Ltd.), aluminum nitrate ($Al(NO_3)_3 \cdot 9H_2O$, 98%, Shanghai Macklin Biochemical Reagent Co. Ltd.), Tetraethylorthosilicate (TEOS, ≥ 28.4 wt. % SiO_2, Shanghai Titan Scientific Co. Ltd.) and chloroplatinic acid (H_2PtCl_6, Shanghai Macklin Biochemical Reagent Co. Ltd.) were all used as received without further purification.

1.2 Synthesis of pentamethonium bromide.

Pentamethonium bromide ($PMBr_2$) was synthesized according to the literature method.[1] 24.63 g of trimethylamine and 11.73 g of 1,5-dibromopentane were mixed in 80 ml of ethanol and homogenized for 0.5 h, and the mixture was refluxed at 333 K for 24 h under N_2 atmosphere. Then, the solvent was evaporated at 313 K and the resulting yellow sticky liquid was washed with ethyl acetate to get white solid product. After drying under vacuum, the SDA was obtained in the form of bromide salt and designated as $PMBr_2$. ^{1}H NMR (600 MHz, D_2O): δ 1.49-1.56 (H4) , 1.90-1.99 (H3), 3.18-3.23 (H1), 3.41-3.46 (H2). ^{13}C NMR (600 MHz, D_2O): δ 22.01-22.73 (C3, C4) , 52.88-53.35 (C1), 65.08-66.55 (C2).

1.3 Synthesis of conventional *MRE zeolites.

For comparison, the conventional ZSM-48 sample were synthesized with $PMBr_2$ as SDA following the literature method.[1] In a typical synthesis, 0.41 g of NaOH, 1.11 g of $Al(NO_3)_3 \cdot 9H_2O$ and 1.65 g of $PMBr_2$ were dissolved in 21.60 g of deionized water and stirred for 6 h before the addition of 6.35 g of TEOS was added at last. The mixture was homogenized by magnetic stirring for 6 h, transferred to a 100 mL Teflon-lined

autoclave to proceed crystallization at 433 K for 96 h under tumbling. The as-synthesized sample was denoted as ZSM-48-$PMBr_2$-x, with the suffix x standing for Si/Al ratio. The product was processed in the same procedure as described in the Synthesis of quasi-crystalline hierarchical ***MRE** Zeolites, except that the calcination temperature was set to be 823 K. The obtained proton-form product was designated as HZSM-48-$PMBr_2$-x.

1.4 Supporting platinum on zeolites.

0.50 wt. % of Pt was loaded on proton-form zeolites via the solution impregnation method. 0.01 g of chloroplatinic acid, 1.00 g proton-form sample and 80.00 g deionized water were mixed in a glass flask with vigorous stirring at room temperature overnight. Then the suspension was evaporated at 353 K and the solid product was collected for further calcination in at 723 K for 3 h. The obtained catalysts were designated as Pt/HZSM-48-(Me_4-C_{6-7})-x and Pt/HZSM-48-$PMBr_2$-x.

1.5 Characterizations.

Powder XRD patterns were collected between 2θ angles of 5 to 50° at a scanning rate of 5° min^{-1} with a Rigaku D/Max 2550 VB/PC diffractometer (40 kV, 100mA) using a Cu Kα (λ = 1.5418 Å) radiation source. FE-SEM were acquired with a NOVA Nano SEM 450 (FEI). TEM were captured on a JEOL JEM-F200 FEG TEM operating at an accelerating voltage of 200 kV. N_2 adsorption-desorption experiments were performed on an ASAP 2020 (Micromeritics, USA). Prior to adsorption measurements, all the samples were degassed at 573 K for 12 h under vacuum. The surface areas were calculated using BET method. Pore-size-distributions were derived from the adsorption branch data using NLDFT method. BJH method was employed to calculate the mesoporous volumes. Mercury intrusion tests were carried out on an AutoPore IV 9500 instrument. The intrusion volumes were measured by increasing step by step with the pressure, and the equilibrium was at each pressure step. Besides, the intrusion measurements started from the vacuum condition (3.4×10^3 Pa) and ended at high pressure (4.3×10^8 Pa), while the extrusion measurements terminated at normal pressure (1.0×10^5 Pa). The intrusion curves as for Washburn equation were used to calculate the pore size distribution. Pyridine

infrared spectroscopy (Py-IR) and NH_3-IR was performed on a Spectrum 100 Fourier-Transform Infrared Spectroscopy spectrometer. All samples were pressed into wafers with a diameter of 1.4 cm and a weight of 20.0 mg, and subsequently treated for 3 h at 723 K under vacuum to remove impurities. The background baselines were collected at 623 K and 423 K successively as the temperature cooling down. The adsorption of pyridine or NH_3 was manipulated at 298 K for 30 min, followed by the desorption at 423 K and 623 K, and IR spectra were recorded simultaneously. The amount of absorbed pyridine was calculated using the integrated area of the corresponding bands with the molar extinction coefficients [$\varepsilon_{Bronsted}$(1545 cm^{-1}) = 1.67 $cm \cdot \mu mol^{-1}$ and ε_{Lewis}(1455 cm^{-1}) = 2.22 $cm \cdot \mu mol^{-1}$].[2] The amount of adsorbed NH_3 was calculated using the integrated area of the corresponding bands with the molar extinction coefficients [$\varepsilon_{Brønsted}$ (1450 cm^{-1}) = 1.47 cm μmol^{-1}, ε_{Lewis} (1630 cm^{-1}) =1.98 cm μmol^{-1})][3]. Inductively Coupled Plasma Atomic Emission Spectrometry (ICP-AES) on an IRIS 1000 instrument was employed to measure the Si/Al ratios. TGA were carried out on TGA 8000 analyzer with heating from room temperature to 373 K, staying for 0.5 h and then heating to 1073 K in air atmosphere at a rate of 10 K min^{-1}. Liquid-state ^{1}H and ^{13}C NMR spectra were recorded by a JEOL spectrometer at 500 MHz. The molecular weight of the bromide form of poly-quaternary ammonium cation was determined using GPC. This analysis was performed with a WATERS 2414 differential refractive index detector, equipped with a WATERS ultra hydrogel × 3 gel column. A 0.10 M aqueous sodium nitrate solution served as the mobile phase, and polyethylene glycol was employed as the standard reference sample. Solid-state ^{1}H MAS NMR, ^{13}C cross-polarization (CP) MAS NMR, ^{27}Al MAS, ^{29}Si MAS NMR, $^{13}C\{^{1}H\}$ HETCOR MAS NMR, $^{27}Al\{^{1}H\}$, and $^{29}Si\{^{1}H\}$ HETCOR MAS NMR were employed, using a Bruker Ascend 600 spectrometer (14.1 T). The resonance frequencies for ^{1}H, ^{27}Al, ^{29}Si and ^{13}C were 600.13 MHz, 156.38 MHz, 119.2 MHz and 150.92 MHz, respectively. The ^{13}C CP MAS NMR spectra were obtained using a 3.2 mm MAS NMR probe, with a spinning rate of 18 kHz, a contact time of 2 ms, and a recycle delay of 2 s. For ^{27}Al MAS NMR experiments, a 3.2 mm probe with a spinning rate of 18 kHz, a $\pi/12$ pulse length of 0.36 μs and a repetition time of 0.5 s were used, referencing the chemical shifts to a 1.00 M $Al(NO_3)_3$ solution. ^{29}Si MAS NMR spectrum was recorded with a 7 mm probe at a spinning rate of 4 kHz, a $\pi/4$ pulse length of 3 μs, and a recycle delay of 45 s, using tetramethylsilane (TMS) as the chemical shift reference. $^{13}C\{^{1}H\}$ HETCOR

experiments were executed at a spinning rate of 18 kHz with a CP contact time of 2 ms and a recycle delay of 2 s. Each t_1 increment was carefully scanned 480 times to ensure precision. Prior to these experiments, all these samples were dehydrated at 353 K under a pressure of < 10^{-3} Pa over 10 h. $^{27}Al^{4}$ HETCOR experiments were executed at a spinning rate of 18 kHz with a CP contact time of 5 ms, a recycle delay of 2 s, and a scan number of 1600 for each t1 increment. $^{29}Si\{^{1}H\}1$. HETCOR experiments were executed at a spinning rate of 18 kHz with a CP contact time of 1.5 ms, a recycle delay of 2 s, and a scan number of 240 for each t_1 increment. The experimental ^{27}Al MAS NMR spectra were fitted using Dmfit which is an NMR software package with several options for simulating the NMR spectra of quadrupolar nuclei fitting of the NMR spectra was done using the built in 2QUAD function, which allows the computation of spectra at finite MAS rates and takes into account 2nd order quadrupolar effects and chemical shift anisotropy.

1.6 Computations.

ZSM-48 (polymorph A) zeolite crystallography data was obtained from International Zeolite Association database (http://www.iza-structure.org/databases/). Density Functional Theory (DFT, Perdew-Burke-Ernzerhof, 96T Periodic Model) was employed to conduct the structural optimization. According to the previous work by Lippmaa et al.,[5, 6] a generally applicable, semiempirical correlation between the ^{27}Al MAS NMR isotropic chemical shift δ_{iso} (in ppm) and the average -Al-O-Si- bond angle θ for a given T sites can be described as:

$$\delta_{iso} = -0.5\theta + 132 \quad (1)$$

δ_{iso}: the ^{27}Al MAS NMR isotropic chemical shift;

θ: the average-Al-O-Si- bond angle.

1.7 Diffusivity property measurements.

The diffusion properties of ZSM-48 samples were measured on an intelligent gravimetric analyzer instrument (IGA-100) with 2-methylhexane (2-MC_6) as the probe molecule. 0.1 g sample was pretreated in N_2 atmosphere at 573 K for 3 h under vacuum (< 10^{-6} Pa) until the sample's weight no longer changed to

remove impurities. Subsequently the sample was cooled to 303 K and the adsorption was operated under a mixture gas consisting of 2-MC_6 and N_2. Isotherms and the corresponding kinetics of adsorption and desorption were obtained at varied partial pressure (P/P_0 = 0-1) steps.

The Fick's second law was used to estimate the effective diffusion coefficient.

$$\frac{\partial C}{\partial t} = D_{eff}\left(\frac{\partial^2 C}{\partial x^2}\right) \tag{2}$$

C: the concentration of 2-MC_6 inside the particle;

t: time;

D_{eff}: the diffusion coefficient;

x: the distance to the center of the slab.

When the adsorption process was at the beginning on a slab-like crystal, the solution of the equation above can be approximated as:

$$\frac{q(t)}{q(\infty)} = \frac{2}{\sqrt{\pi}} \cdot \sqrt{\frac{D_{eff}}{R^2}} \cdot \sqrt{t} \tag{3}$$

$q(t)/q(\infty)$: the normalized 2-MC_6 uptake;

R: the characteristic diffusion length.

1.8 Catalytic performance evaluations.

N-dodecane (n-C_{12}) hydroisomerization was performed in a fixed-bed reactor. The zeolite sample (0.70 g, 20-40 mesh) was activated at 723 K for 3 h at a heating rate of 2 K min^{-1} under a flow of H_2 (37 mL min^{-1}) and cooled down to reaction temperature. The reaction was carried out at between temperature range of 463 K to 593 K and weight hourly space velocity (WHSV) of 0.75 $g_{n\text{-dodecane}}$ g_{cat}^{-1} h^{-1}. The effluent product gas composition was analyzed periodically using an on-line gas chromatograph (GC) equipped with a flame ionization detector (FID) and a HP-PONA capillary column (50 m × 2 μ m × 0.5 μm). Two sets of data at each reaction temperature were averaged to present the actual catalytic capability.

2. Supplementary Figures

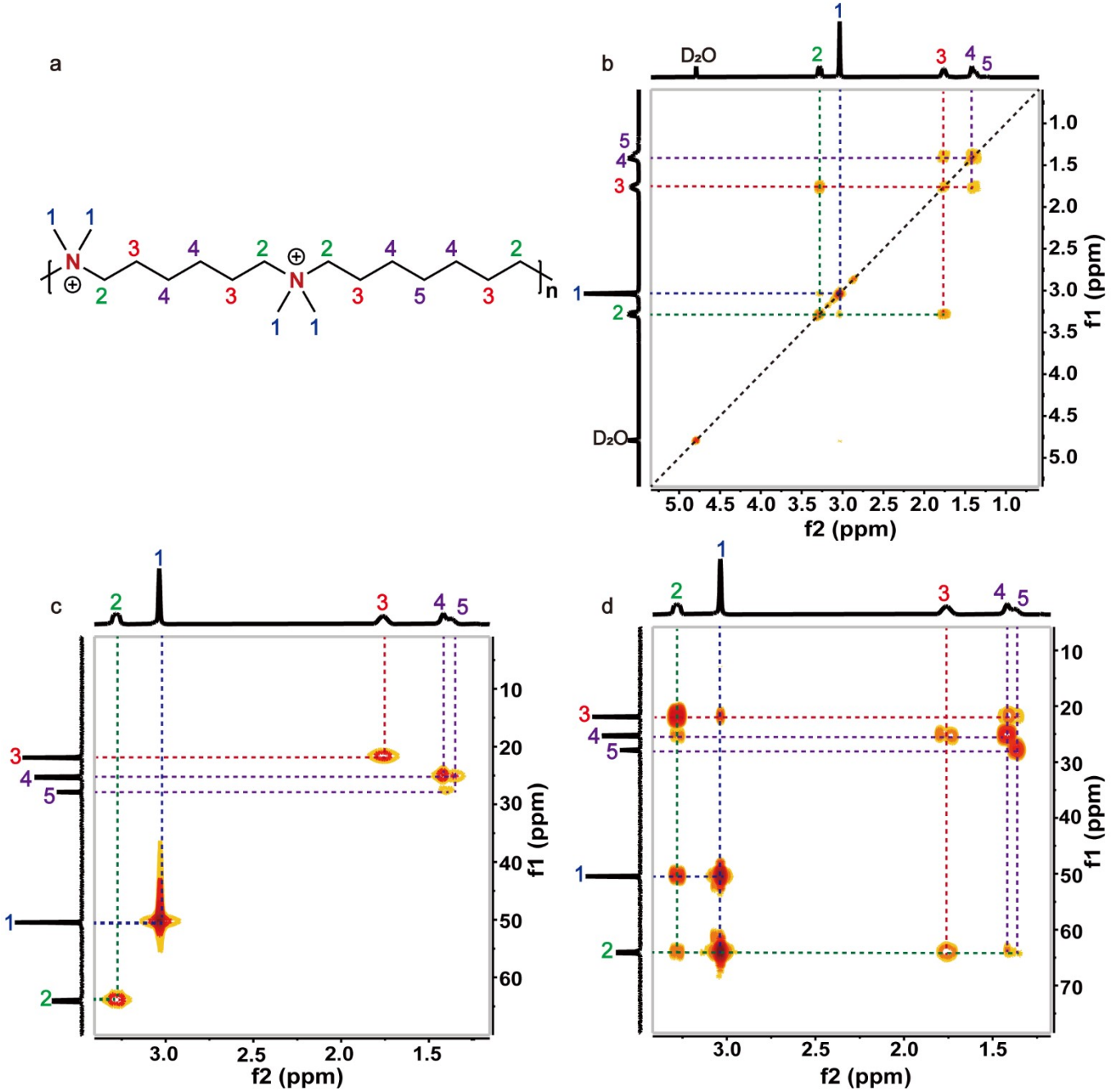

Figure S1. NMR correlation spectroscopy of the polycationic SDA Me_4-$C_{6\text{-}7}$. (a) Structural model of the polycationic SDA Me_4-$C_{6\text{-}7}$, with labelled atoms corresponding to the correlation spectroscopy. (b) ^{1}H-^{1}H correlation spectroscopy (COSY), showing the correlation between hydrogen nuclei within 3 covalent bonds. (c) $^{13}C\{^{1}H\}$ heteronuclear single-quantum correlation spectroscopy (HSQC), evidencing the correlation between hydrogen and carbon nuclei within 1 covalent bond. (d) $^{13}C\{^{1}H\}$ heteronuclear multiple bond correlation spectroscopy (HMBC), revealing the correlation between hydrogen and carbon nuclei within 2-3 covalent bonds NMR spectra of Me_4-$C_{6\text{-}7}$ dissolved in D_2O. The linkage of the polymeric chain agrees well with the determined correlations.

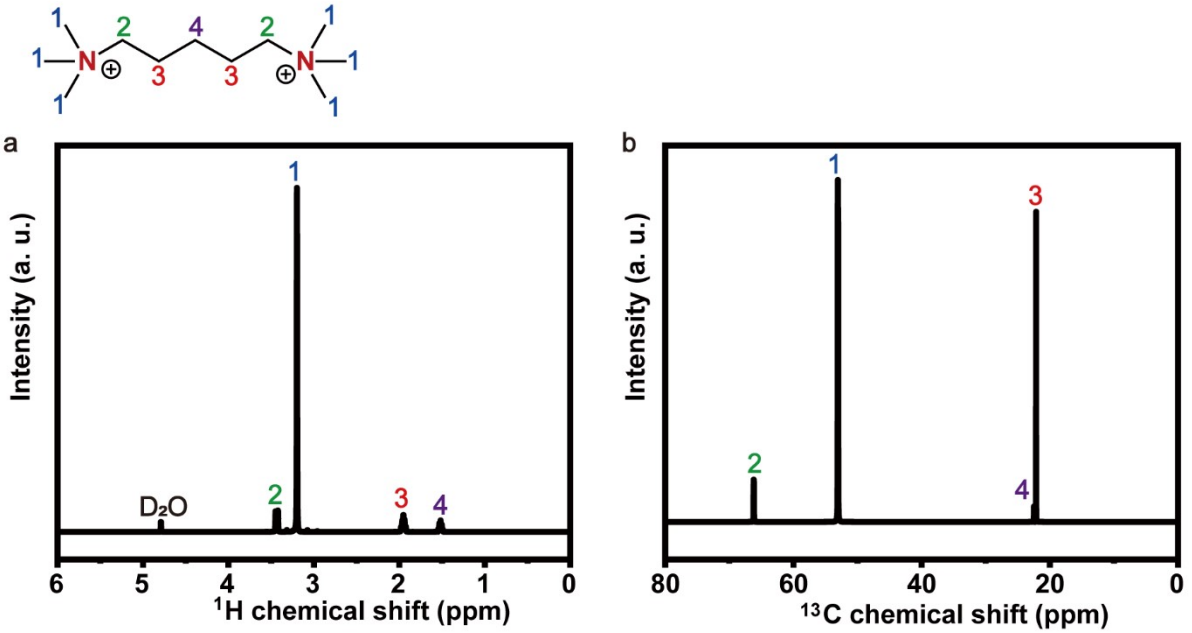

Figure S2. Structural characterization of $PMBr_2$. (a) ^1H NMR spectra of $PMBr_2$ dissolved in D_2O. (b) ^{13}C NMR spectra of $PMBr_2$ dissolved in D_2O.

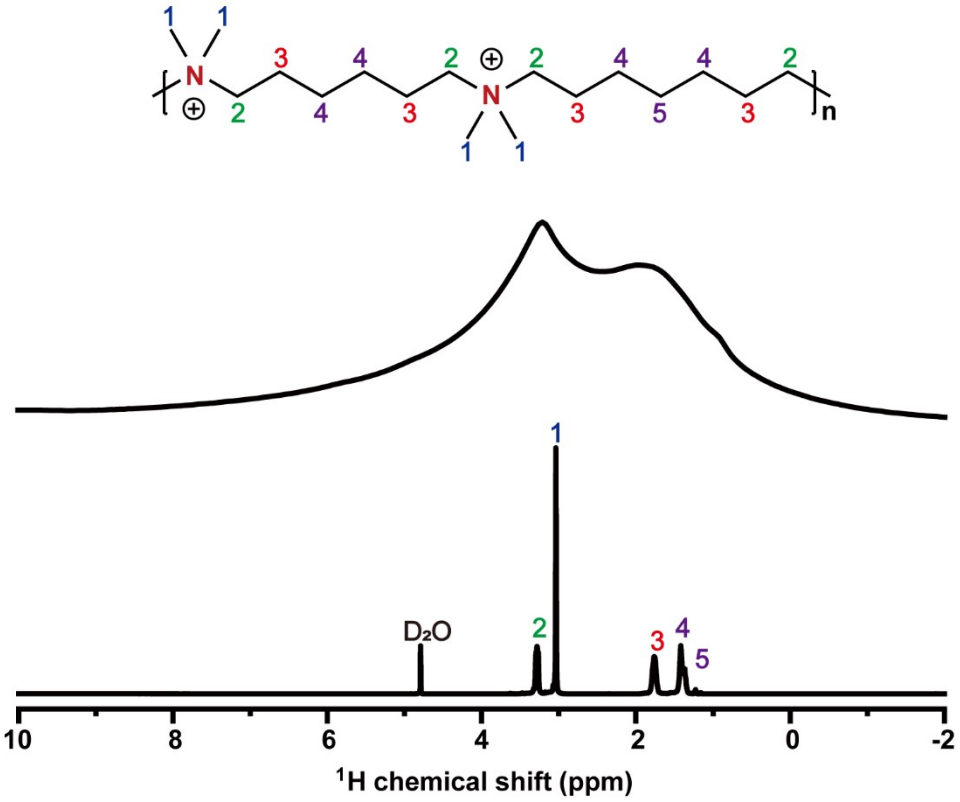

Figure S3. ^{1}H MAS NMR spectrum of ZSM-48-(Me_4-$C_{6\text{-}7}$)-30 with Me_4-$C_{6\text{-}7}$ occluded in the framework (upper) and ^{1}H NMR spectrum of Me_4-$C_{6\text{-}7}$ in D_2O solution (bottom). ^{1}H MAS NMR of as-synthesized ZSM-48-(Me_4-$C_{6\text{-}7}$)-30 show signals near 1.5-1.8 ppm and 3.0-3.2 ppm assigned to H3-5 and H1-2, in line with the ^{1}H NMR of Me_4-$C_{6\text{-}7}$ in D_2O solution.

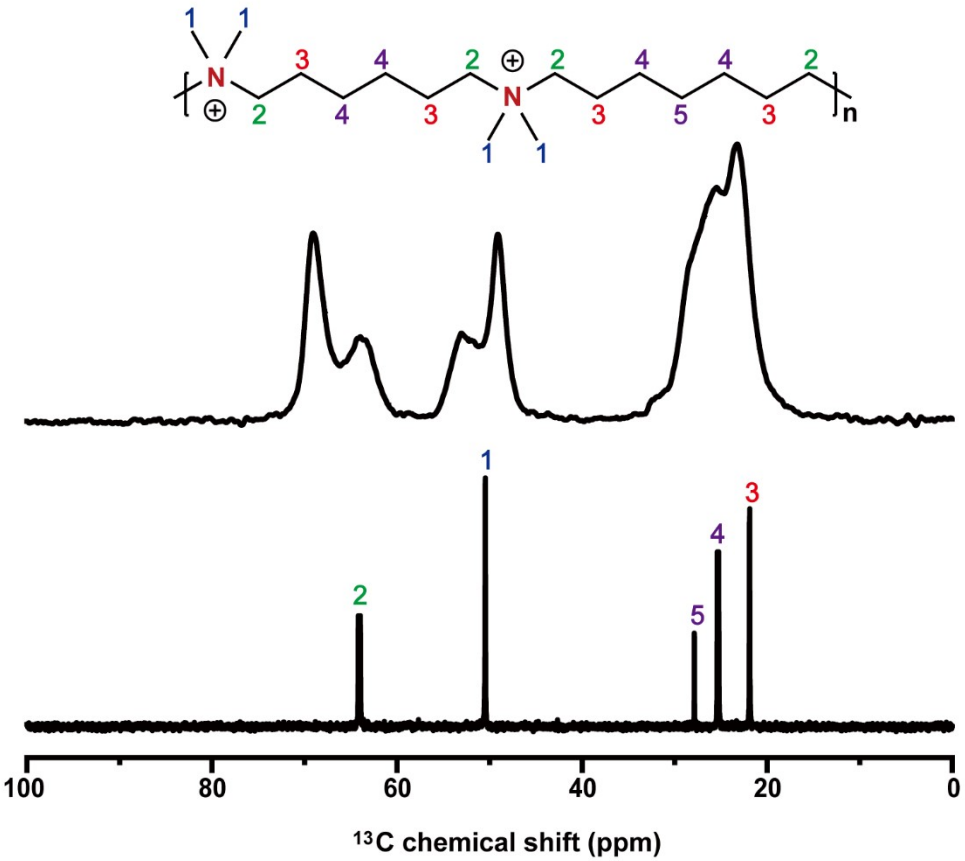

Figure S4. ^{13}C cross-polarization magic angle spinning (CP MAS) NMR spectrum of ZSM-48-(Me_4-C_{6-7})-30 with Me_4-C_{6-7} occluded in the framework (upper) and ^{13}C NMR spectrum of Me_4-C_{6-7} in D_2O solution (bottom). ^{13}C MAS NMR of as-synthesized ZSM-48-(Me_4-C_{6-7})-30 show signals near 23-32, 49-53 and 65-69 ppm assigned to C3-5, C1 and C2, in line with the ^{13}C NMR of Me_4-C_{6-7} in D_2O solution. The confinement effect of the framework on Me_4-C_{6-7} changed the chemical environment of C1 and C2, resulting in splitting of the corresponding peaks.

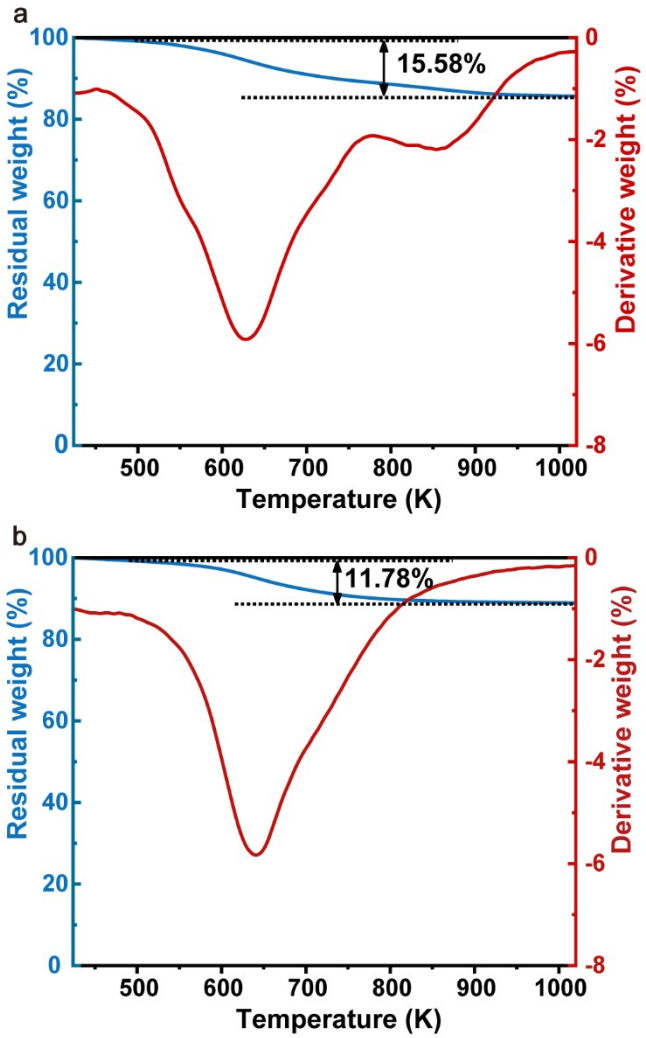

Figure S5. Thermogravimetric analysis (TGA) curves of (a) as-synthesized ZSM-48-(Me_4-$C_{6\text{-}7}$)-30 and (b) ZSM-48-$PMBr_2$-30. TGA curve of ZSM-48-(Me_4-$C_{6\text{-}7}$)-30 shows a major exothermic peak at ca. 630 K, due to the combustion of SDAs in the zeolite micropores, and a broad exothermic peak at ca. 863 K, which is related to the condensation of the surface silanols.[7] ZSM-48-$PMBr_2$-30 only shows one exothermic peak at ca. 640 K. Compared with the weight loss of 11.78 wt. % for ZSM-48-$PMBr_2$-30, more Me_4-$C_{6\text{-}7}$ (15.58 wt. %) have been detected in ZSM-48-(Me_4-$C_{6\text{-}7}$)-30, owing to a strong interaction of the polycationic SDA with the inorganic framework.

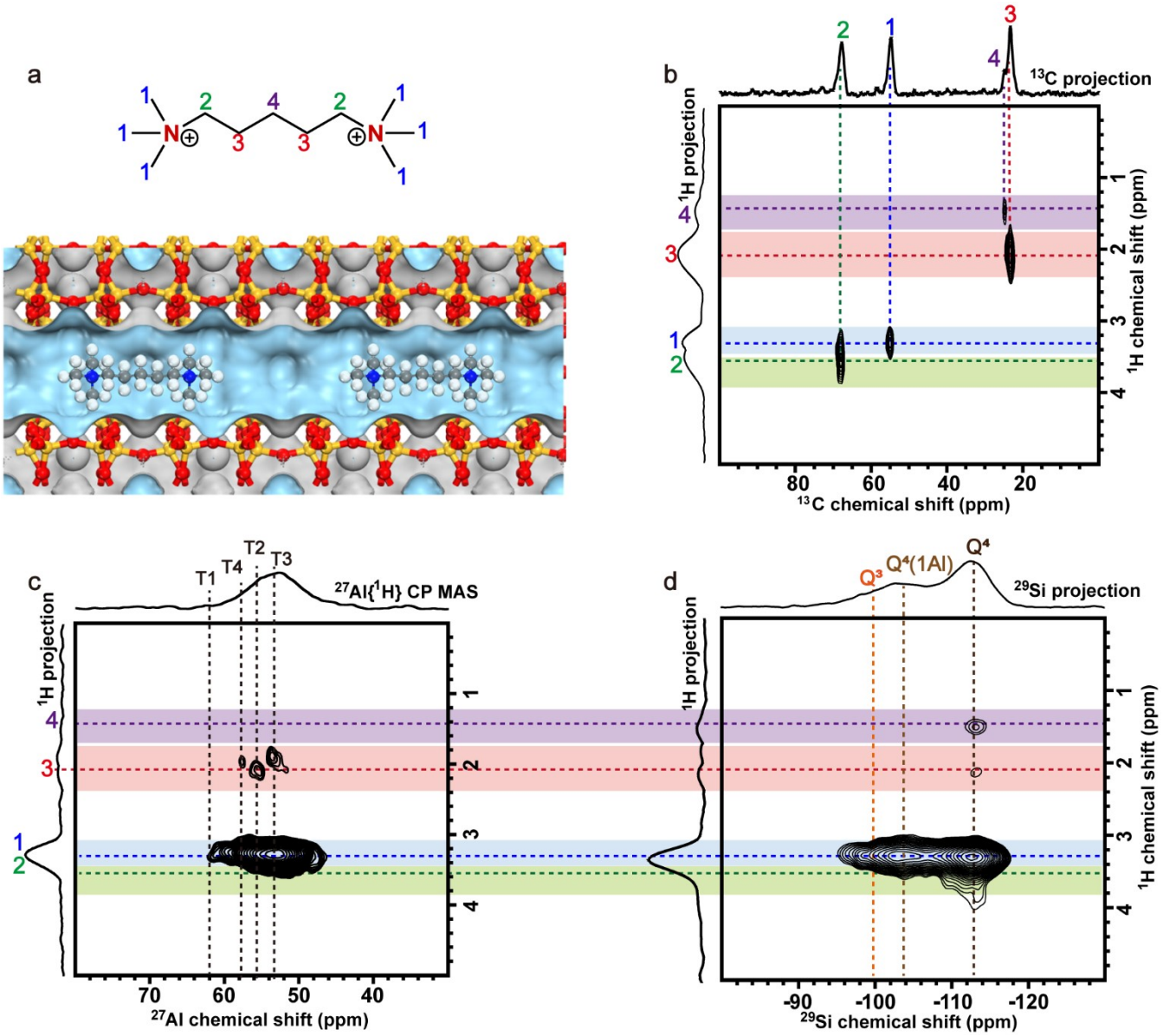

Figure S6. (a) Structure of ZSM-48 with occluded $PMBr_2$ along the pore axis. (b) Solid-state 2D $^{13}C\{^1H\}$ HETCOR spectra of as-synthesized ZSM-48-$PMBr_2$-30 with a $^{13}C\{^1H\}$ contact time of 0.5 ms. (c) $^{27}Al\{^1H\}$ HETCOR spectra of as-synthesized ZSM-48-$PMBr_2$-30 with a $^{27}Al\{^1H\}$ contact time of 2 ms (c). (d) $^{29}Si\{^1H\}$ HETCOR spectra of as-synthesized ZSM-48-$PMBr_2$-30 with a $^{29}Si\{1H\}$ contact time of 5 ms. C1 (55 ppm), C2 (68 ppm), C3 (23 ppm) and C4 (25 ppm) atoms are related with H1 (3.3 ppm), H2 (3.5 ppm), H3 (2.1 ppm) and H4 (1.4 ppm) atoms, respectively. The correlations between H and C from occluded $PMBr_2$ in ZSM-48-$PMBr_2$-30 prove that $PMBr_2$, instead of the decomposed molecules act as SDA during the hydrothermal synthesis. H1 and H2 atoms near quaternary ammonium are highly correlated to Al at 53-62 ppm, as well as Q^3 and Q^4 species, while H atoms on methylene chain far from quaternary ammonium show weak interactions with Al at 53-58 ppm and Q^4 = [**Si**-$(OSi)_4$] species.

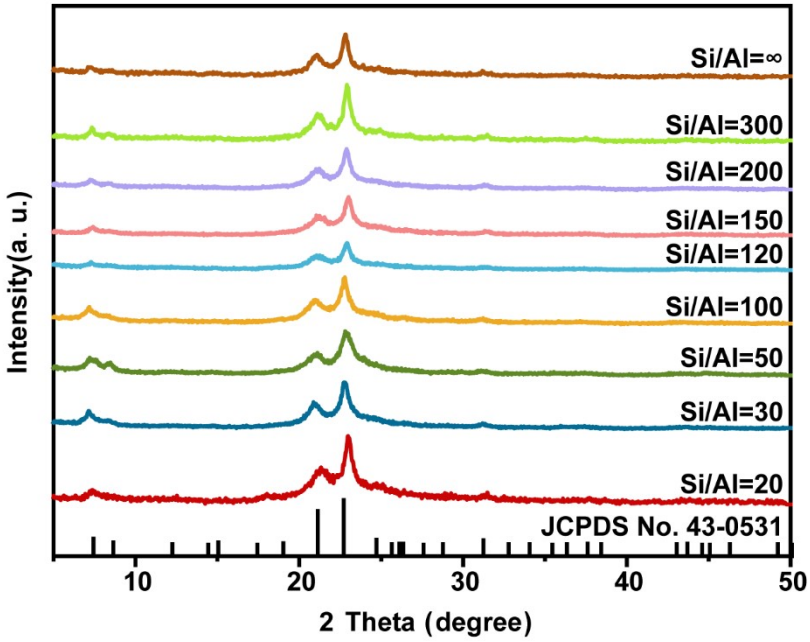

Figure S7. XRD patterns (λ = 1.5418 Å) for ZSM-48-(Me_4-C_{6-7}) of varied Si/Al ratios. The syntheses were carried out from reaction mixtures of 30 SiO_2: 0.75-∞ Al_2O_3: 1.5 Me_4-C_{6-7}: 10 NaOH: 1200 H_2O under static condition at 423 K for 120-216 h, as summarized in Table S4, entries 1-9. Pure ***MRE** phase can be crystallized with regulatable Si/Al ratio of 20-∞, as revealed by product composition analysis (Table S2). Here, it is noteworthy that ***MRE** zeolite often crystallizes in siliceous form (typically Si/Al >100) using other types of SDAs (Table S1), and the composition window has been markedly widened by using Me_4-C_{6-7}.

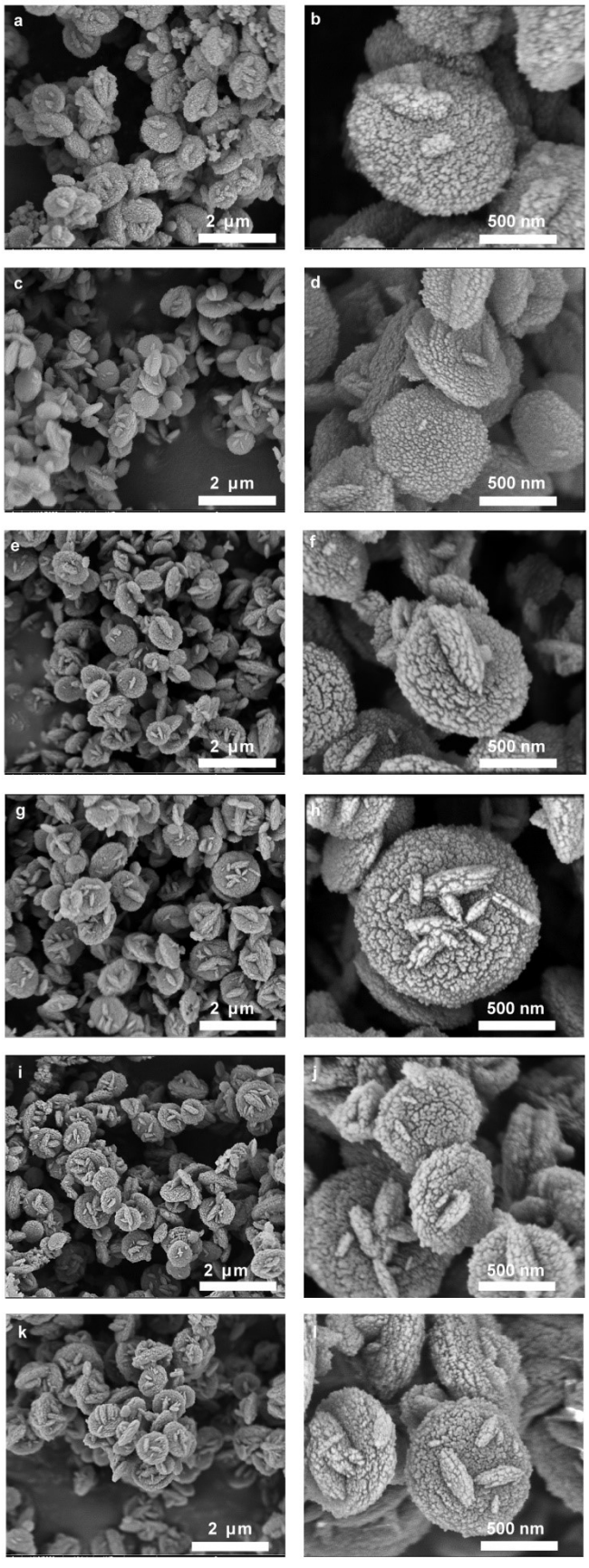

(To be continued)

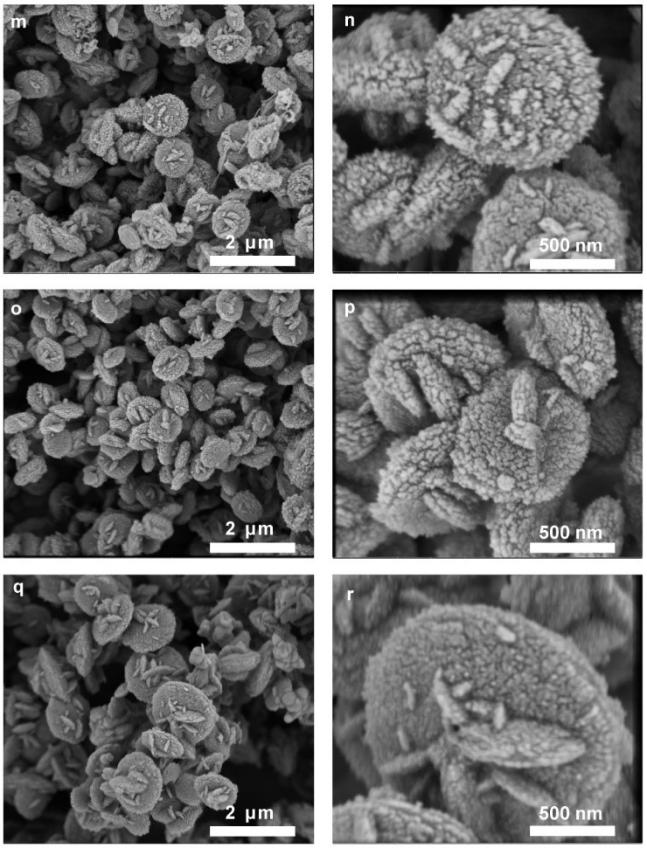

Figure S8. Morphology of ZSM-48-(Me_4-$C_{6\text{-}7}$) with varied Si/Al ratios. FE-SEM micrographs (a-b: Si/Al = 20; c-d: Si/Al = 30; e-f: Si/Al = 50; g-h: Si/Al = 100; i-j: Si/Al = 120; k-l: Si/Al = 150; m-n: Si/Al = 200; o-p: Si/Al = 300; q-r: Si/Al = ∞) for ZSM-48-(Me_4-$C_{6\text{-}7}$) with varied Si/Al ratios synthesized from reaction mixtures of 30 SiO_2: 0.75-∞ Al_2O_3: 1.5 Me_4-$C_{6\text{-}7}$: 10 NaOH: 1200 H_2O. FE-SEM micrographs disclose that the discus-like morphology is invariant to changes of Si/Al ratio in the starting gels.

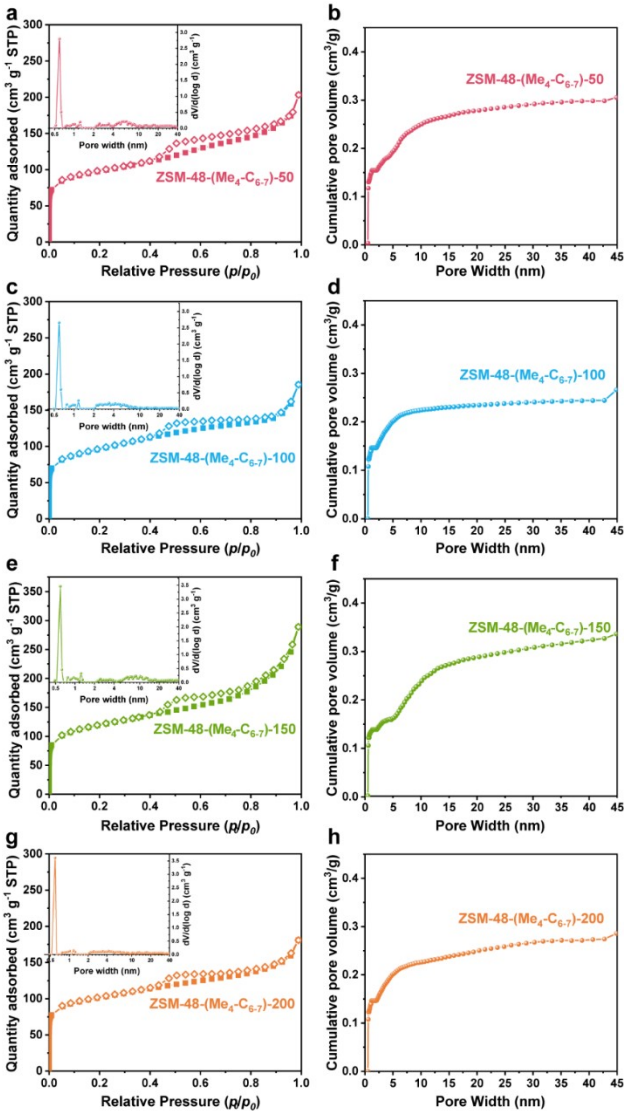

Figure S9. N_2 physisorption isotherms (a, c, e, g), cumulative pore volume (b, d, f, h) and pore size distribution (inset of a, c, e and g) inferred from NLDFT method utilizing the adsorption branch of the isotherm for calcined ZSM-48-(Me_4-C_{6-7})-50, ZSM-48-(Me_4-C_{6-7})-100, ZSM-48-(Me_4-C_{6-7})-150 and ZSM-48-(Me_4-C_{6-7})-200.

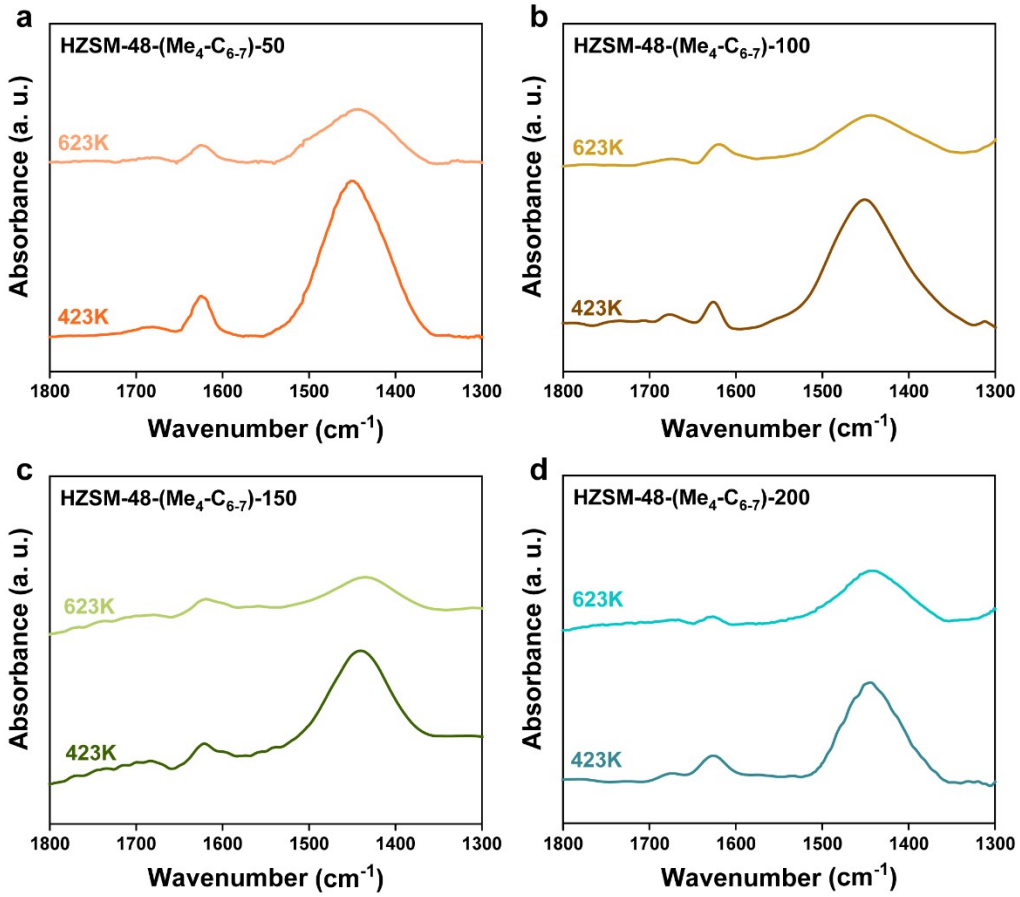

Figure S10. NH_3-IR of NH_3 adsorbed on HZSM-48-(Me_4-C_{6-7})-50 (a), HZSM-48-(Me_4-C_{6-7})-100 (b), HZSM-48-(Me_4-C_{6-7})-150 (c) and HZSM-48-(Me_4-C_{6-7})-200 (d) zeolites at 423 and 623 K.

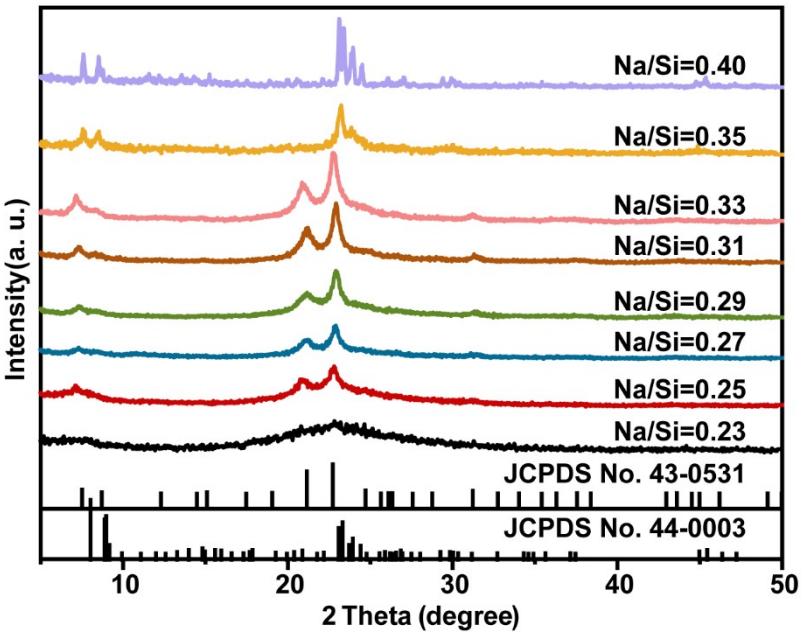

Figure S11. XRD pattern (λ = 1.5418 Å) for ZSM-48-(Me_4-C_{6-7}) derived from varied Na^+/Si ratios. The syntheses were carried out from reaction mixtures of 30 SiO_2: 0.5 Al_2O_3: 1.5 Me_4-C_{6-7}: 6.9-12 NaOH: 1200 H_2O under static condition at 423 K for 72-240 h (Table S4 entries 2 and entries 10-16). Alkaline cations always work synergistically with SDAs in the crystallization of zeolites. To investigate the effect of NaOH content, a batch composition of 30 SiO_2: 0.5 Al_2O_3: 1.5 Me_4-C_{6-7}: y NaOH: 1200H_2O, with Na^+/Si ratio ranging from 0.23 to 0.40, was adopted. Pure ***MRE** zeolite can be obtained for Na^+/Si ratio from 0.25-0.33. Prolonged crystallization time (from 120 h to 216 h) is required with decreased of Na^+/Si ratio (from 0.33 to 0.25), for the lacking of mineralizer OH^-. Only amorphous materials can be obtained when Na^+/Si ratio is 0.23, even after 240 h of heating at 423 K. When the Na^+/Si ratio is increased higher than 0.35, pure ZSM-5 zeolite was generated, indicating that excessive Na^+ disfavors formation of ***MRE** phase.[1]

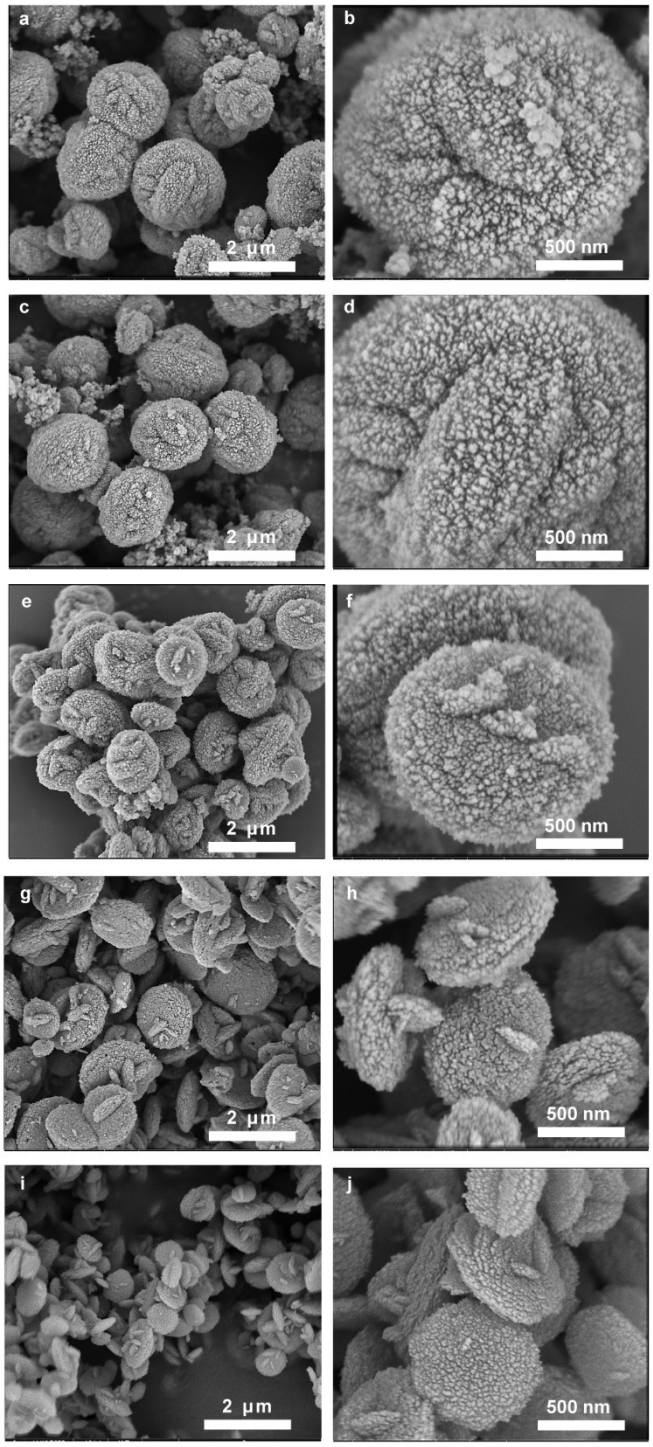

Figure S12. Morphology of ZSM-48-(Me_4-C_{6-7}) with varied Na^+/Si ratios. FE-SEM micrographs (a-b: Na^+/Si = 0.25; c-d: Na^+/Si = 0.27; e-f: Na^+/Si = 0.29; g-h: Na^+/Si = 0.31; i-j: Na^+/Si = 0.33) for ZSM-48-(Me_4-C_{6-7}) derived from synthetic gel of molar composition of 30 SiO_2: 0.5 Al_2O_3: 1.5 Me_4-C_{6-7}: 6.9-12 NaOH: 1200 H_2O. The change of Na^+/Si ratio led to considerable changes in the phase selectivity and product morphology. The discus-shaped crystals have grown thicker (from 100-200 nm to 1-2 µm) and larger (from 500-900 nm to 600-800 nm across the disk) with decreasing Na^+/Si ratio. Indeed, close to spheroid shape has been observed when Na^+/Si is kept as low as 0.25, while the diameter and thickness of ZSM-48 crystals increases significantly.

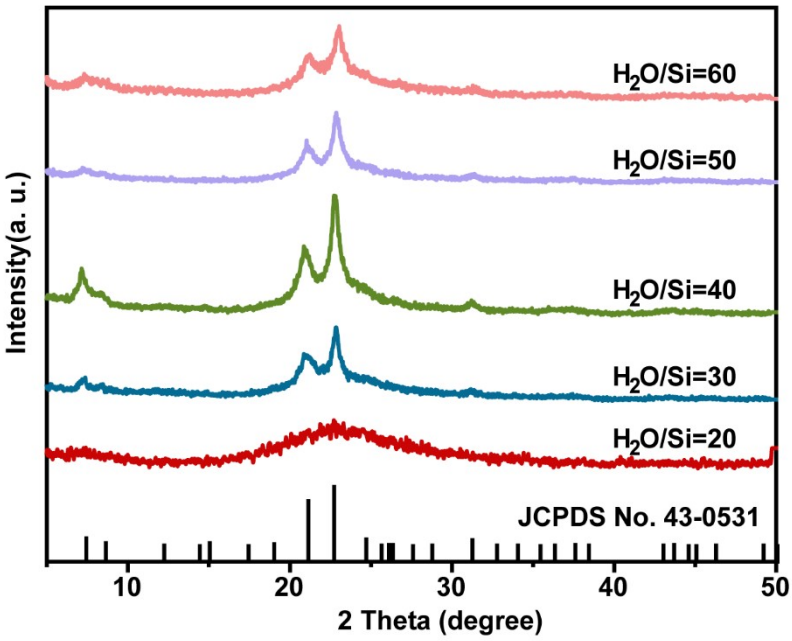

Figure S13. XRD pattern (λ = 1.5418 Å) for ZSM-48-(Me_4-C_{6-7}) derived from varied H_2O/Si ratios. The syntheses were carried out from reaction mixtures of 30 SiO_2: 0.75-∞ Al_2O_3: 1.5 Me_4-C_{6-7}: 10 NaOH: 600-1800 H_2O under static condition at 423 K for 120-240 h (Table S4, entries 2 and 17-20). Pure ***MRE** phase is synthesizable within the H_2O/Si ratio of 30-60. It is likely that the polycationic SDA could hardly be solubilized at concentrated gel (H_2O/Si = 20), and only amorphous product was collected even after prolonged crystallization time of 240 h. It is plausible that crystal growth is favored over nucleation when diluted gel is adopted, hence, less numbers of nuclei have been produced and their further growth are favored for the presence of sufficient nutrients.[8]

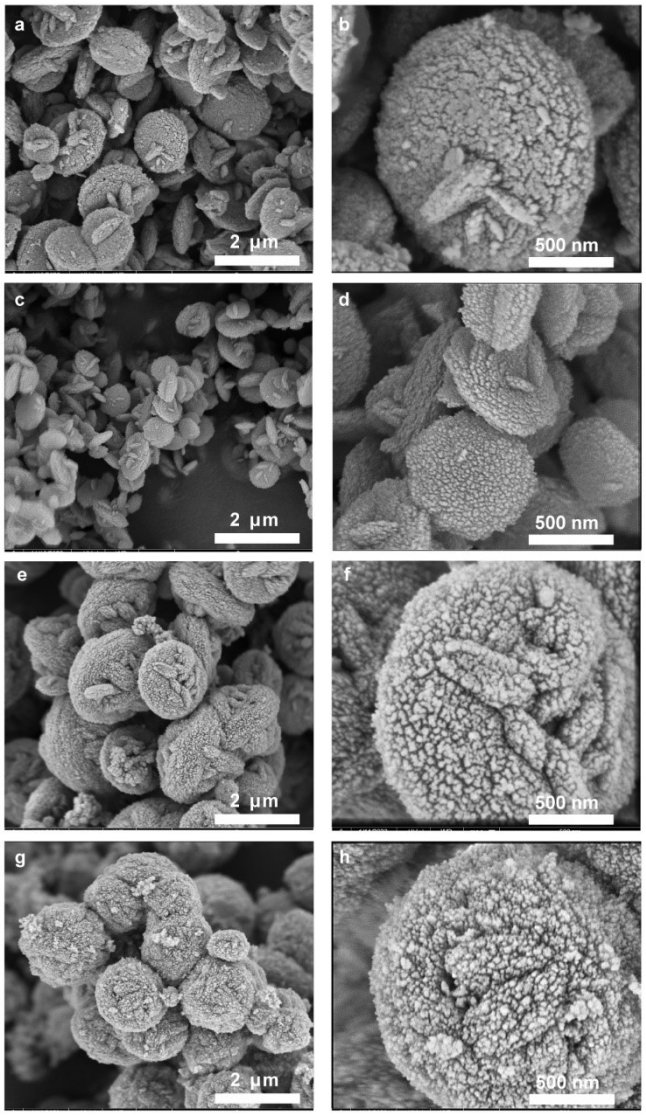

Figure S14. Morphology of ZSM-48-(Me_4-C_{6-7}) derived from varied H_2O/Si ratios. FE-SEM micrographs for ZSM-48-(Me_4-C_{6-7}) zeolites (a-b: H_2O/Si = 30; c-d: H_2O/Si = 40; e-f: H_2O/Si = 50; g-h: H_2O/Si = 60) derived from synthetic gel of 30 SiO_2: 0.5 Al_2O_3: 1.5 Me_4-C_{6-7}: 10 NaOH: 600-1800 H_2O. The FE-SEM micrographs manifest that the same discus-like shape could be attained in the range of H_2O/Si ratio of 30-40, while diluted syntheses produced bulky, spheroid-shaped crystals (1.8-2.3 µm across the disk and 600-650 nm of thickness).

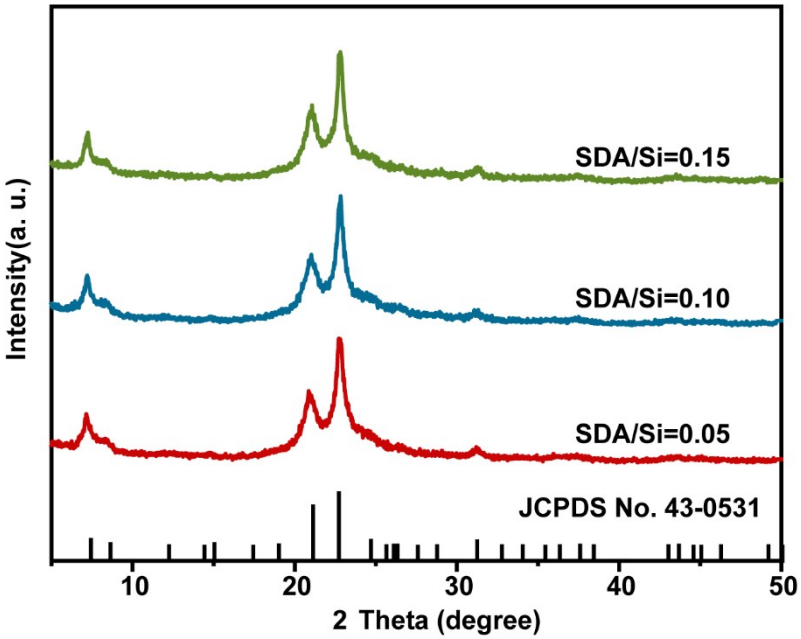

Figure S15. XRD patterns (λ = 1.5418 Å) for ZSM-48-(Me_4-C_{6-7}) derived from varied SDA/Si ratios. The syntheses were carried out from reaction mixtures of 30 SiO_2: 0.75-∞ Al_2O_3: 1.5-4.5 Me_4-C_{6-7}: 10 NaOH: 1200 H_2O under static condition at 423 K. The impact of SDA/Si ratio is found to be marginal when manipulated from 0.05 to 0.15, out of a batch of 120 h (Table S4, entries 2 and 21-22). Overall, the use of polycationic Me_4-C_{6-7} permits the generation of the decagonal symmetry related packing of alike discus-shaped morphology from a broad synthetic composition, thus revealing the strong structure and morphology directing effect of Me_4-C_{6-7}.

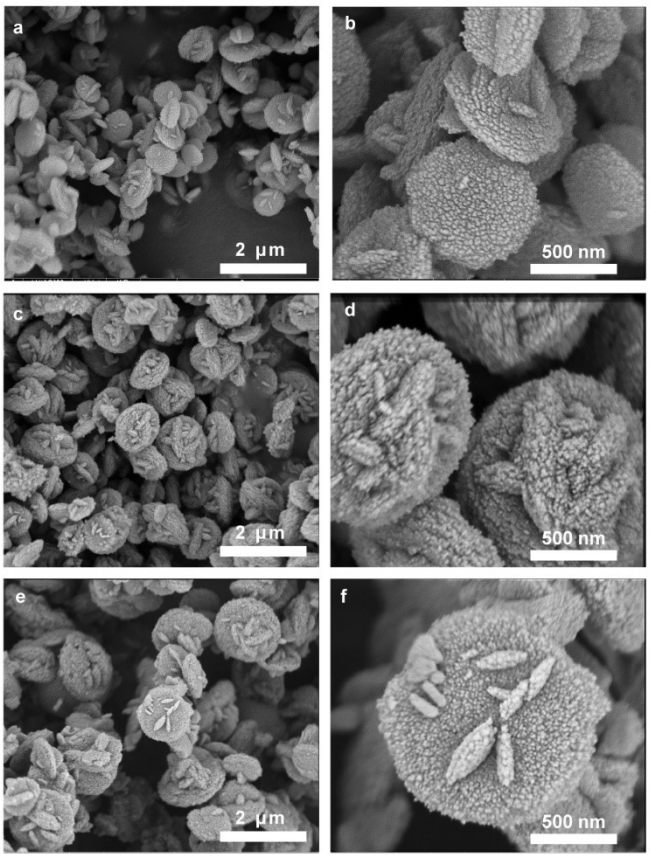

Figure S16. Morphology of ZSM-48-(Me_4-C_{6-7}) derived from varied SDA/Si ratios. FE-SEM micrographs (a-b: SDA/Si = 0.05; c-d: SDA/Si = 0.10; e-f: SDA/Si = 0.15) for ZSM-48-(Me_4-C_{6-7}) derived from synthetic gel of molar composition: 30 SiO_2: 0.5 Al_2O_3: 1.5-4.5 Me_4-C_{6-7}: 10 NaOH: 1200 H_2O.

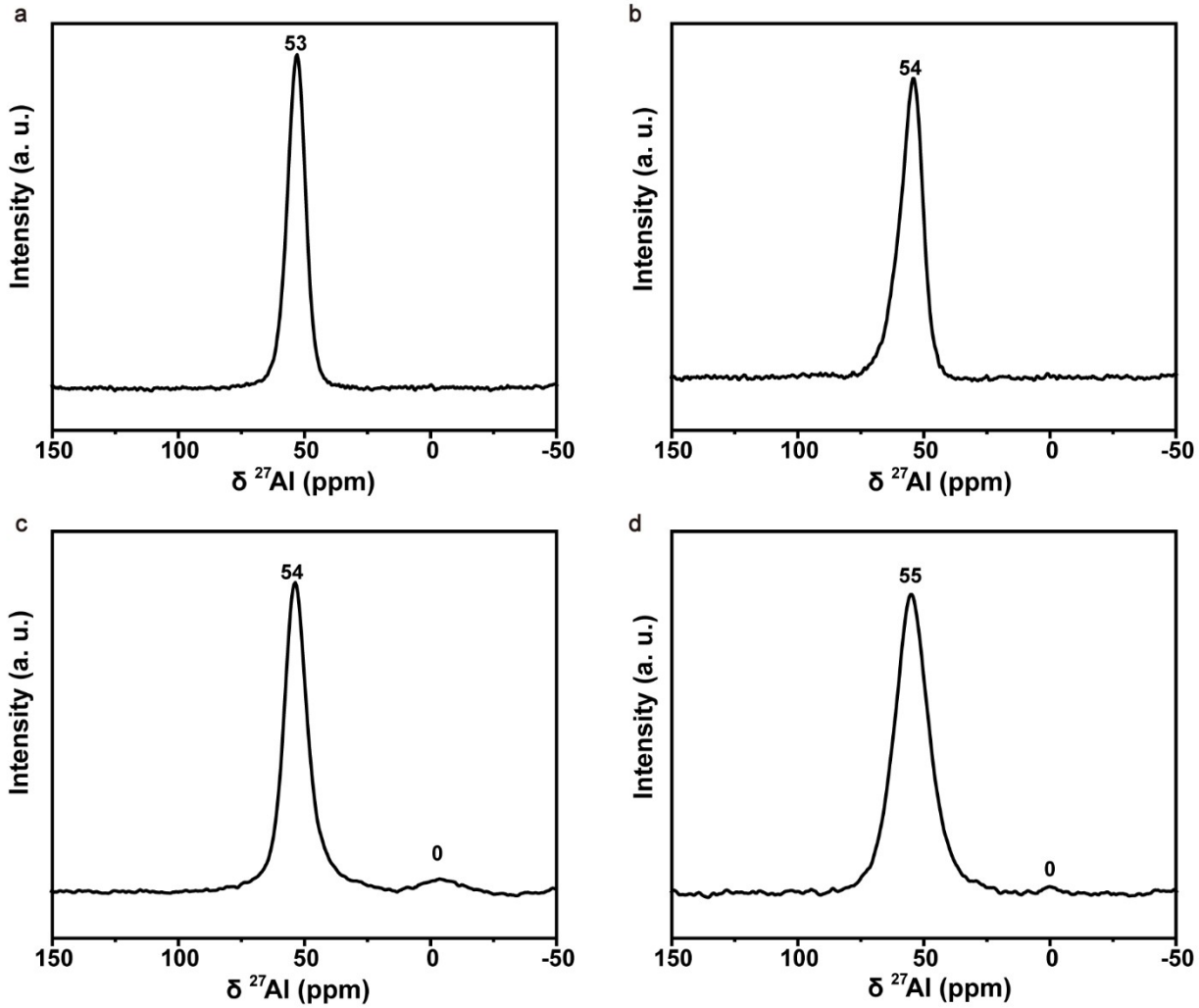

Figure S17. (a) ^{27}Al MAS NMR spectra for as-synthesized ZSM-48-(Me_4-C_{6-7})-30. (b) ^{27}Al MAS NMR spectra for as-synthesized ZSM-48-$PMBr_2$-30. (c) ^{27}Al MAS NMR spectrum for calcined ZSM-48-(Me_4-C_{6-7})-30. (d) ^{27}Al MAS NMR spectrum for calcined ZSM-48-$PMBr_2$-30. The ^{27}Al MAS NMR spectrum for as-synthesized ZSM-48-(Me_4-C_{6-7})-30 and ZSM-48-$PMBr_2$-30 consists only one peak ca. 53-54 ppm, confirming the solely presence of tetrahedrally coordinated, framework AlO_4^- species.[9] The ^{27}Al MAS NMR spectra for calcined ZSM-48-(Me_4-C_{6-7})-30 and ZSM-48-$PMBr_2$-30 consists one intense peak ca. 54-55 ppm, confirming the predominant presence of tetrahedrally coordinated, framework AlO_4^- species. The weak peak at ca. 0 ppm can be assigned to extra framework Al with octahedral coordination, resulting from dealumination in the calcination process.

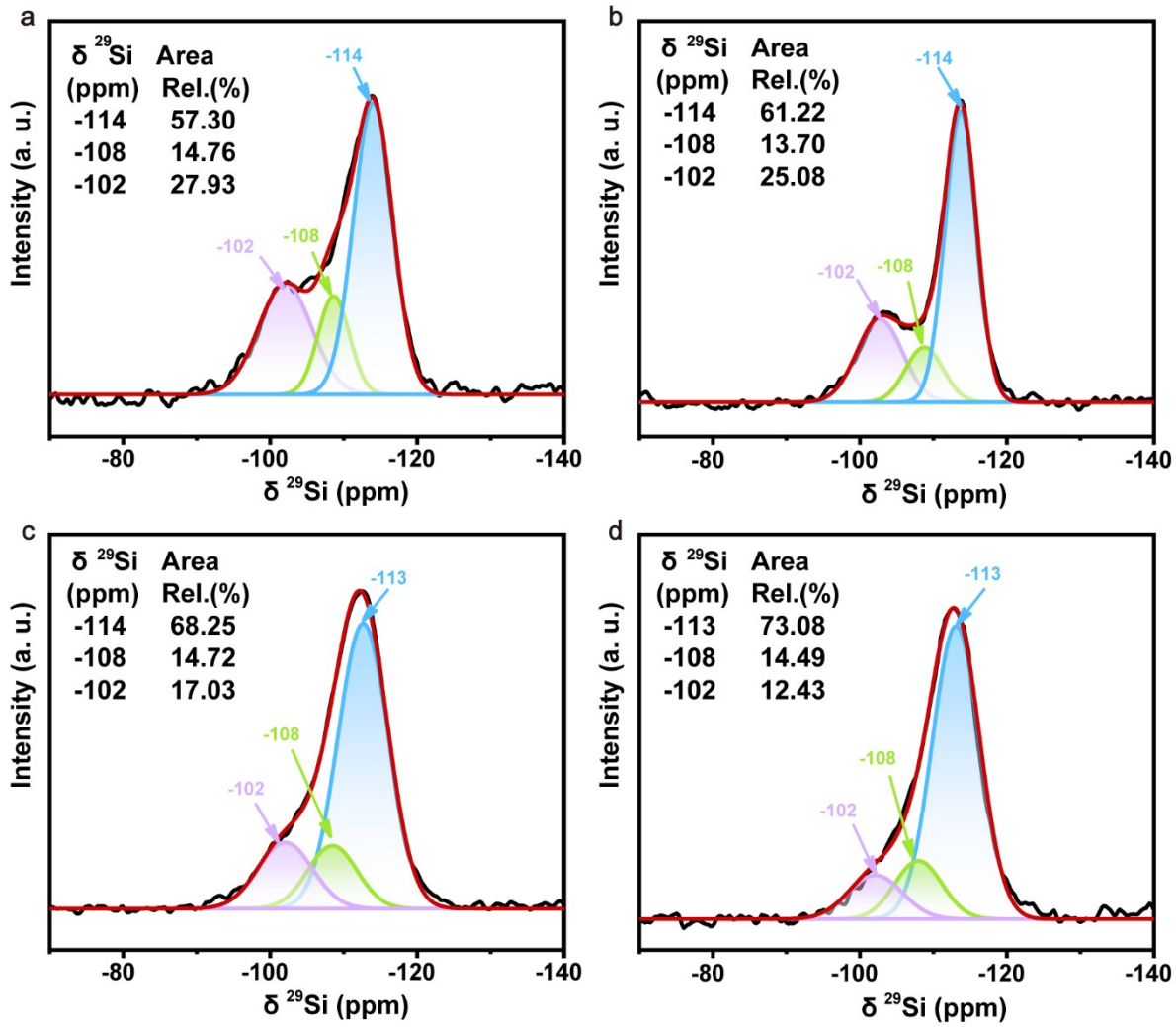

Figure S18. (a) ^{29}Si MAS NMR spectrum for as-synthesized ZSM-48-(Me_4-$C_{6\text{-}7}$)-30. (b) ^{29}Si MAS NMR spectrum for as-synthesized ZSM-48-$PMBr_2$-30. (c) ^{29}Si MAS NMR spectrum for calcined ZSM-48-(Me_4-$C_{6\text{-}7}$)-30. (d) ^{29}Si MAS NMR spectrum for calcined ZSM-48-$PMBr_2$-30. ^{29}Si MAS NMR spectra of as-synthesized samples can be deconvoluted into three peaks centered at ca. -114 ppm, -108 ppm and -102 ppm, assignable to Q^4 = [**Si**-$(OSi)_4$], framework Q^4 = [**Si**-$(OSi)_3(OAl)$] species, and surface Q^3 = [**Si**-$(OSi)_3(OH)$] species,[10] respectively, verifying that they are incorporated into the zeolite framework. ^{29}Si MAS NMR spectra of calcined samples can be deconvoluted into three peaks centered at ca. -113 ppm, -108 ppm and -102 ppm, assignable to Q^4 = [**Si**-$(OSi)_4$], framework Q^4 = [**Si**-$(OSi)_3(OAl)$] species, and surface Q^3 = [**Si**-$(OSi)_3(OH)$] moieties,[10] respectively. The broadening of the asymmetric resonance peak observed in calcined samples can be explained by the occupation of Al on varied T sites, as also corroborated by 2D ^{27}Al 3Q MAS NMR spectra (Fig. 3).

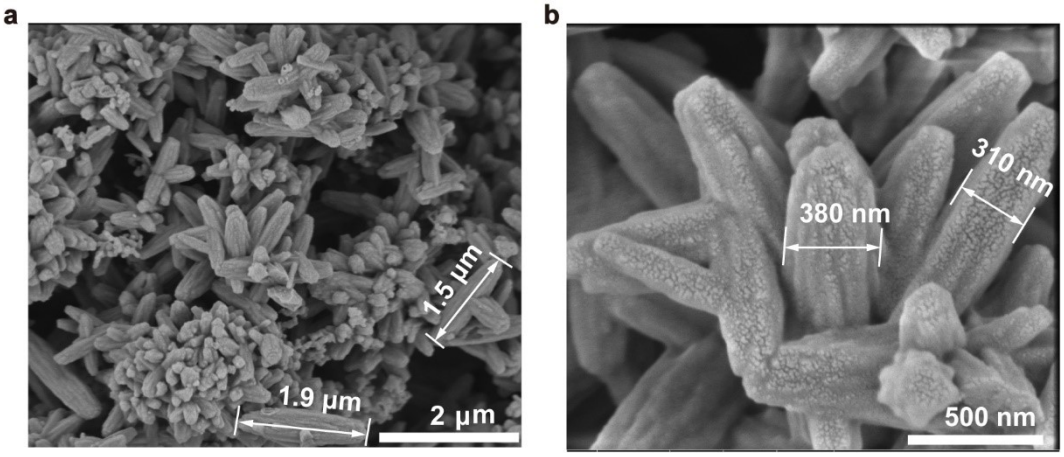

Figure S19. FE-SEM micrographs for calcined ZSM-48-PMBr$_2$-30. ZSM-48-PMBr$_2$-30 comprises of spindle-shaped particles, typically 1-2 µm in length and 300-500 nm in width.

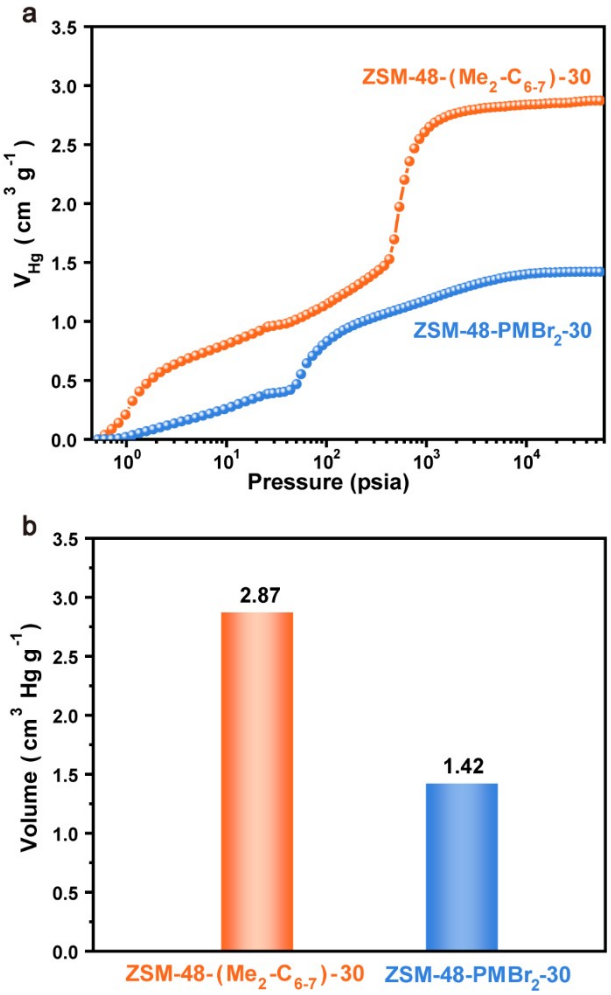

Figure S20. Mercury intrusion measurements of macro-/meso- pore size of calcined ZSM-48 samples. Mercury intrusion curves (a) and pore volumes (b) obtained from mercury intrusion measurements for calcined ZSM-48-(Me_4-C_{6-7})-30 and ZSM-48-$PMBr_2$-30 samples. The corresponding pore-size-distribution data are reported in Fig. 1f.

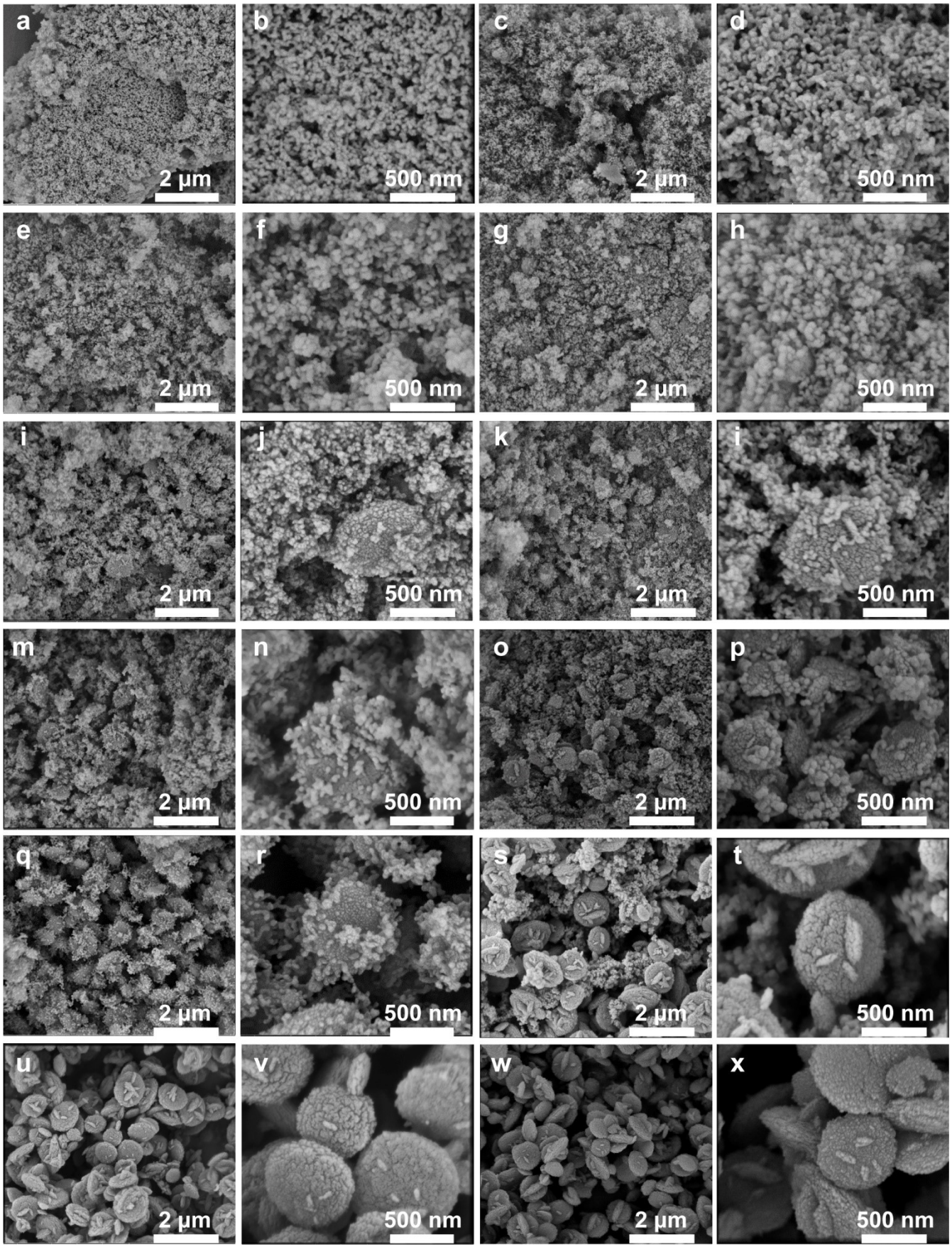

Figure S21. Time-dependent FE-SEM micrographs (a-x) (a-b: 6 h; c-d: 48 h; e-f: 72 h; g-h 84 h; i-j: 86 h; k-l:88 h; m-n: 90 h; o-p: 92 h; q-r: 94 h; s-t: 96 h; u-v: 108 h; w-x:120 h) for ZSM-48-(Me_4-$C_{6\text{-}7}$)-30.

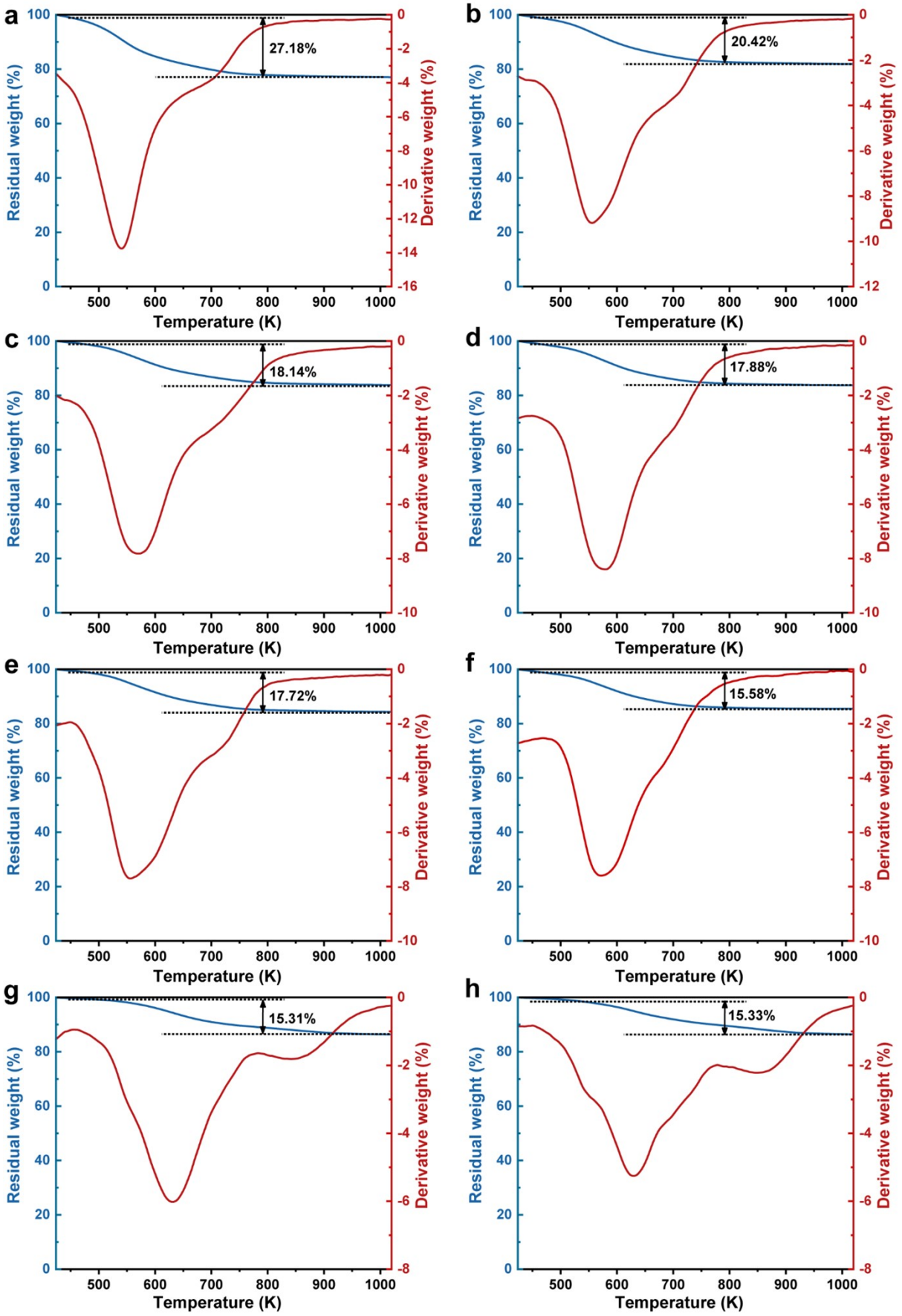

Figure S22. TGA measurements of collected intermediate solids (a-h) (a: 0 h; b: 6 h; c: 48 h; d 84 h; e: 90 h; f: 94 h; g: 108 h; h: 114 h).

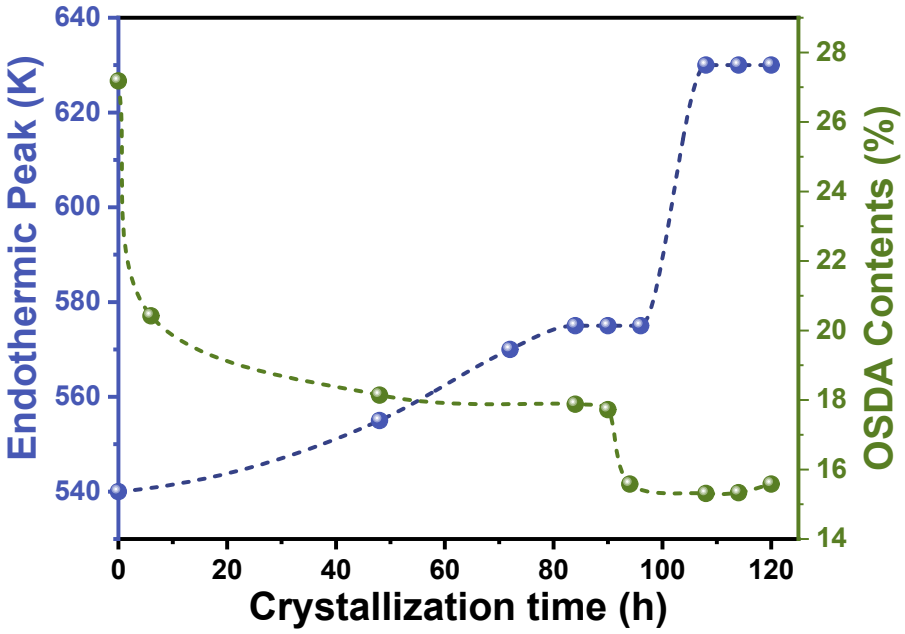

Figure S23. Exothermic peak temperatures and SDA contents for intermediate solid products for ZSM-48-(Me_4-$C_{6\text{-}7}$)-30 in the course of crystallization.

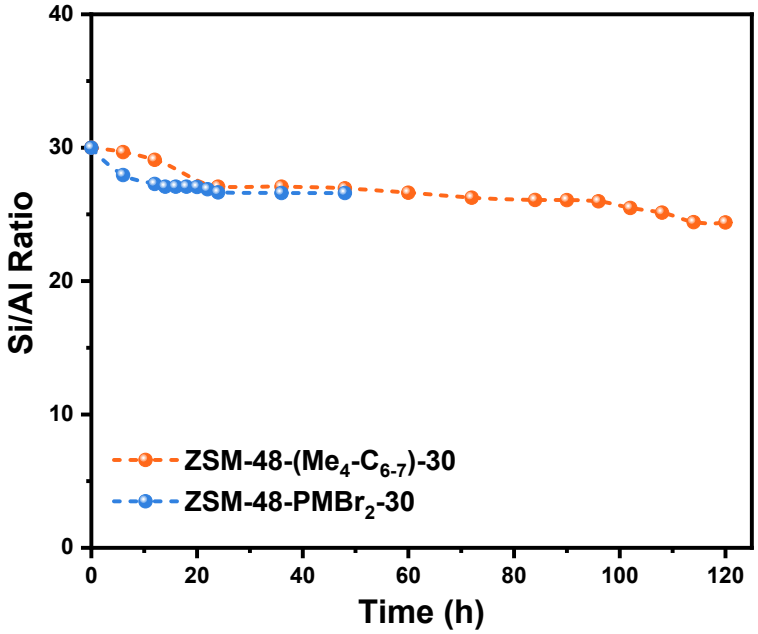

Figure S24. Time-dependent Si/Al ratios for ZSM-48-(Me_4-$C_{6\text{-}7}$)-30 and ZSM-48-$PMBr_2$-30.

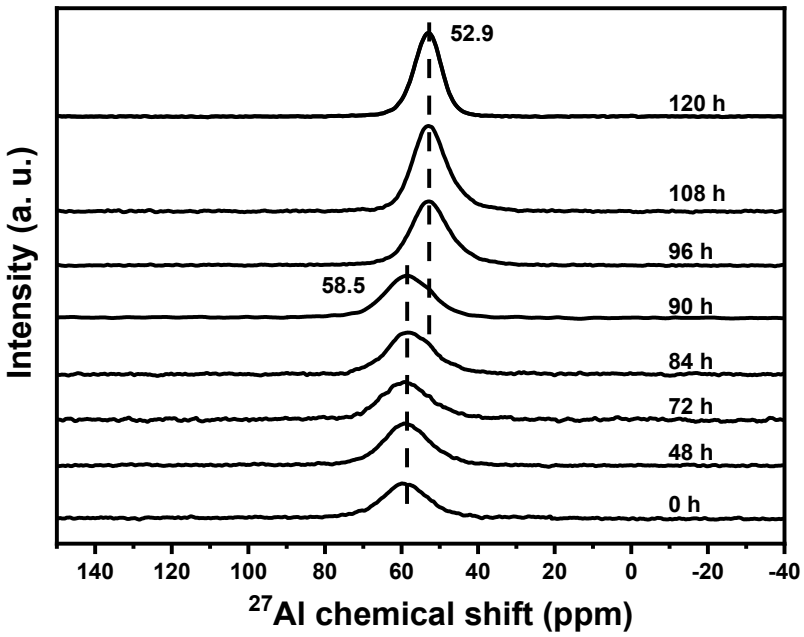

Figure S25. ^{27}Al MAS NMR spectra for ZSM-48-(Me_4-C_{6-7})-30 in the course of crystallization.

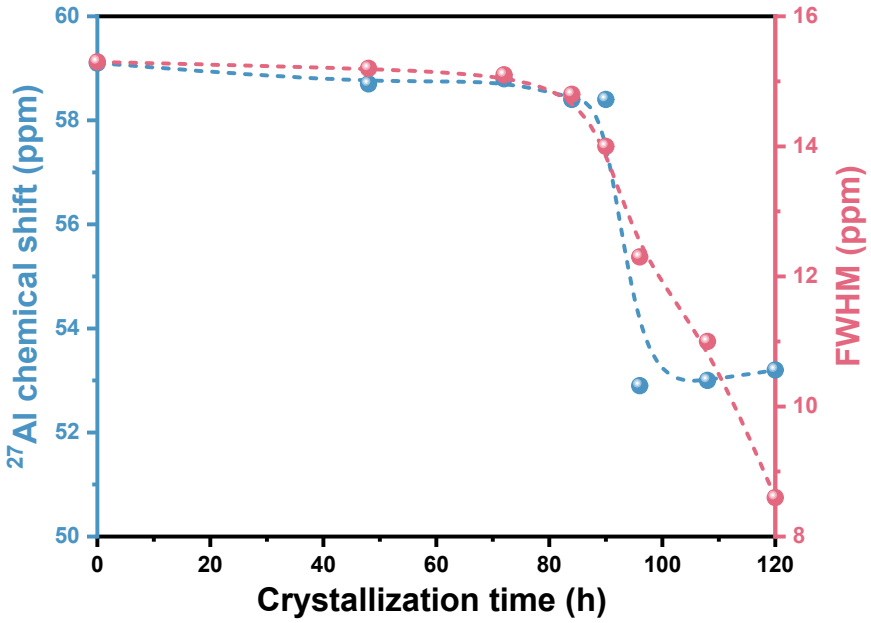

Figure S26. Time-dependent chemical shift and full-width-at-half maximum (FWHM) of ^{27}Al MAS NMR for ZSM-48-(Me_4-$C_{6\text{-}7}$)-30.

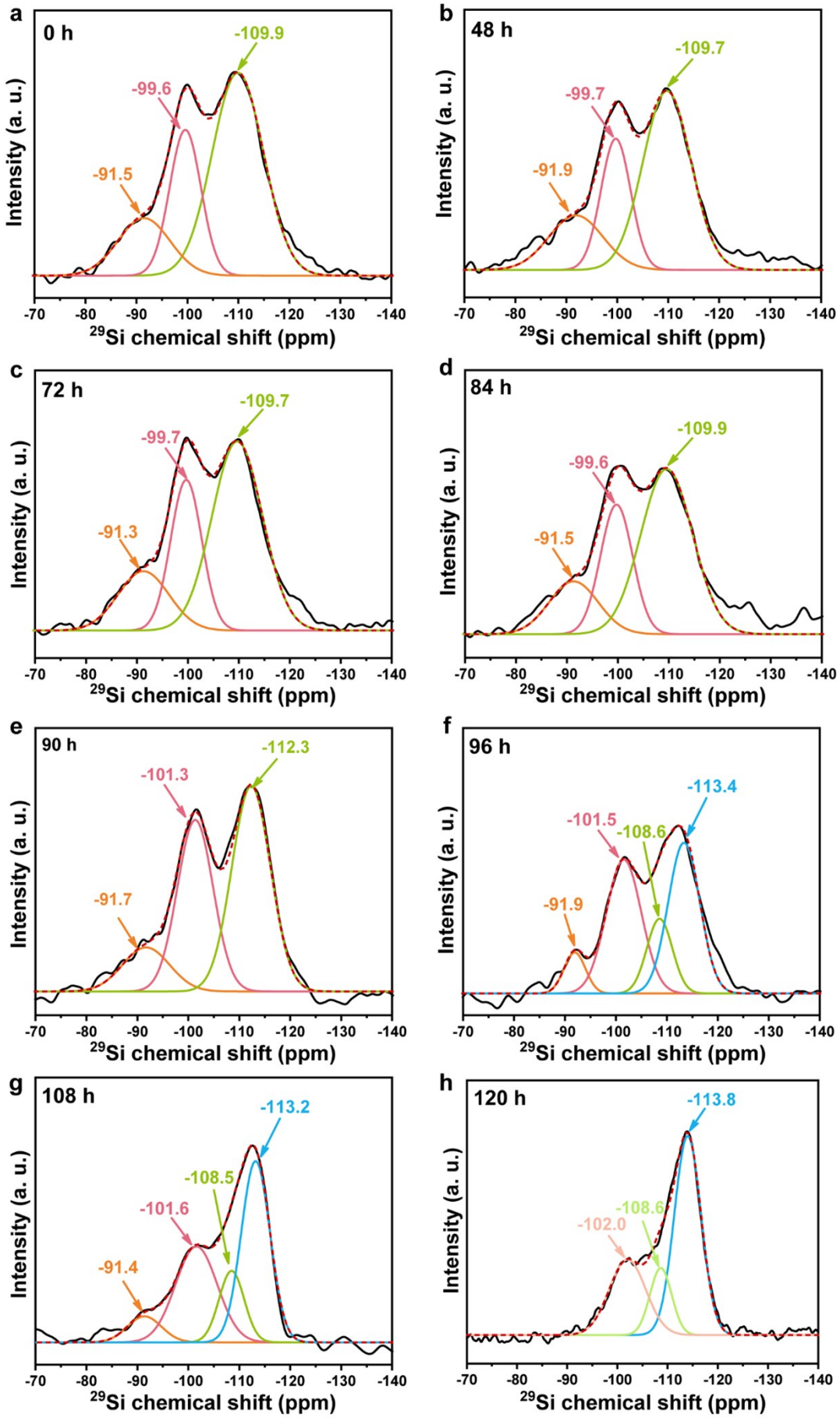

Figure S27. ^{29}Si MAS NMR spectra for ZSM-48-(Me_4-C_{6-7})-30 in the course of crystallization.

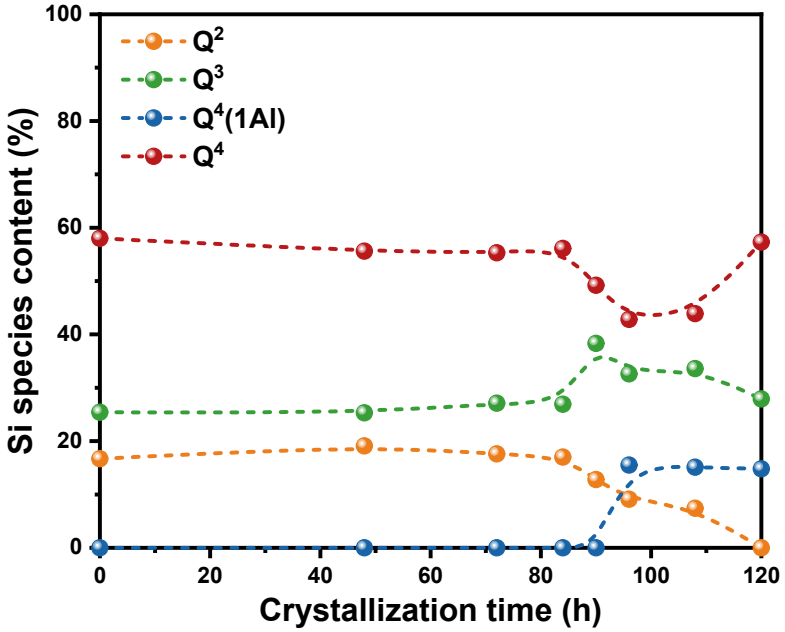

Figure S28. The structural information (a) and the overall Q^3/Q^4 ratio (b) versus crystallization time variations according to ^{29}Si MAS NMR spectra for ZSM-48-(Me_4-$C_{6\text{-}7}$)-30 in the course of crystallization.

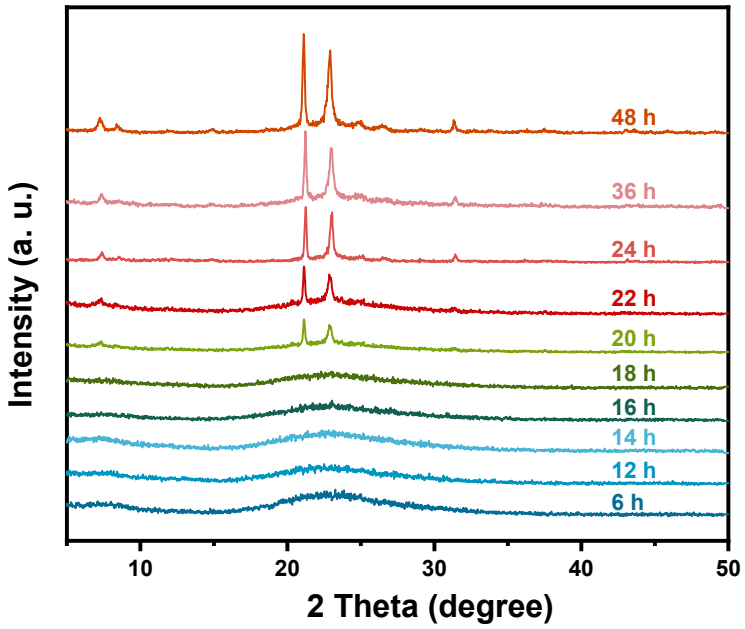

Figure S29. Time-dependent XRD patterns during the course of crystallization obtained at varied periods for ZSM-48-PMBr$_2$-30. In the initial 18 h, no obvious diffraction peak could be observed by XRD, and then a swift increase in crystalline structure was observed before reaching saturation at 48 h.

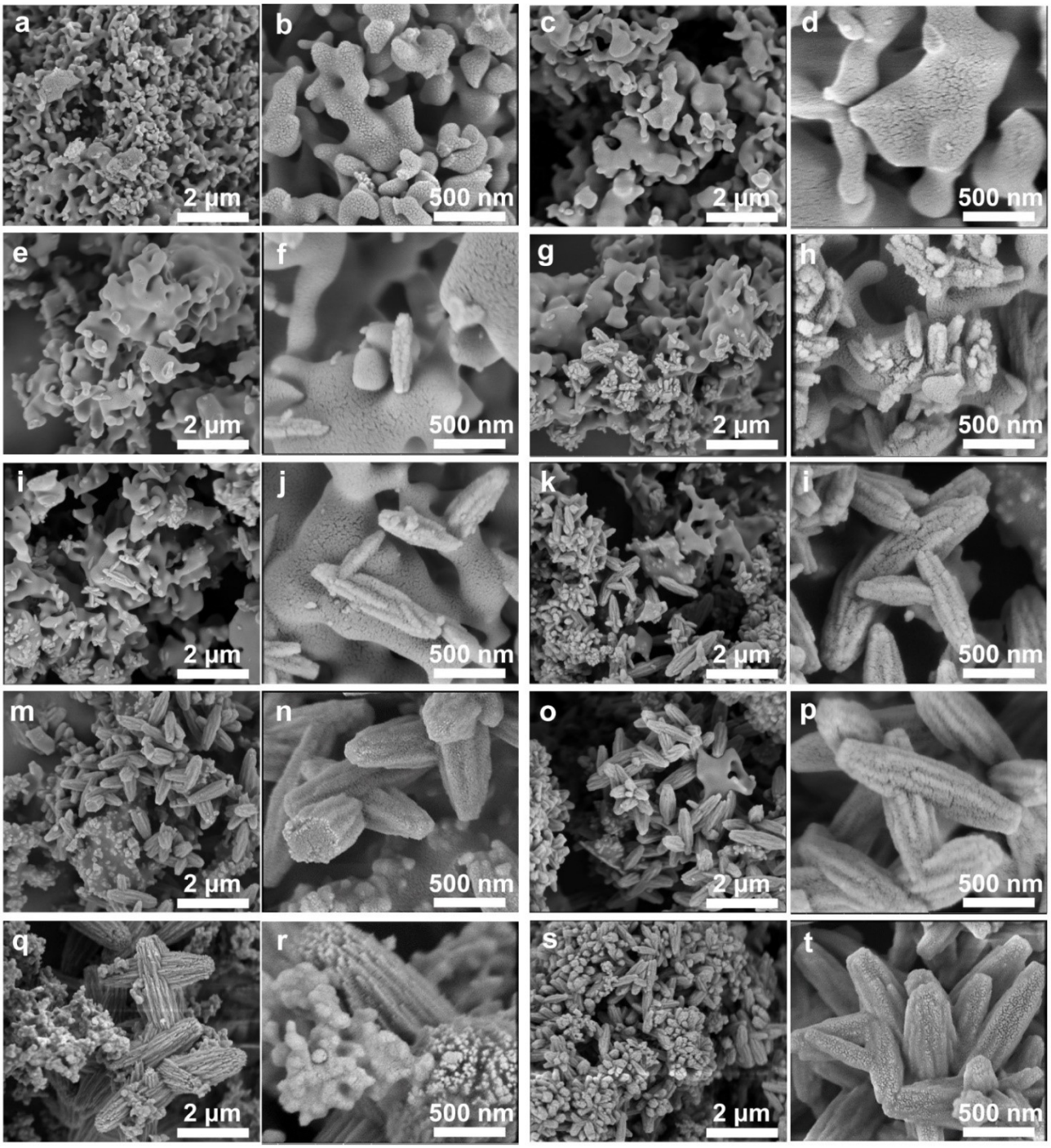

Figure S30. Time-dependent FE-SEM micrographs (a-t) (a-b: 6 h; c-d: 12 h; e-f: 14 h; g-h:16 h; i-j: 18 h; k-l: 20 h; m-n: 22 h; o-p: 24 h; q-r: 36 h; s-t: 48 h) for ZSM-48-$PMBr_2$-30. A rather short induction time of 12 h was identified and nucleation started at 14 h, tiny nuclei with length of ca. 500 nm and width of ca. 150 nm could be observed at the interface between worm-like particles of raw materials and the mother liquor. The nucleus size grew to the length of ca. 800 nm and width of ca. 200 nm at 16 h, and the intergrowth of primary crystals can be observed. The nucleation and crystal growth were found to overlap with that of depolymerization of amorphous species, which was typical for zeolite crystallization in classical nucleation frame.[11] Between crystallization time of 14-18 h, the amounts and crystal size of nuclei increased distinctly. The precursors stayed amorphous, depolymerizing to feed continuous growth of crystals, and rapid crystal growth was observed from 18 to 20 h. Most of the ingredients depolymerized and nuclei grew to bulk crystal with size of 0.6-1.0 μm at 20 h. A series of events, including formation of worm-like particles due to gelation, nucleation at the boundary particles, crystal growth at the expense of these particles are observed to overlap temporally, which is typical for crystallization via the classical mechanism.[12]

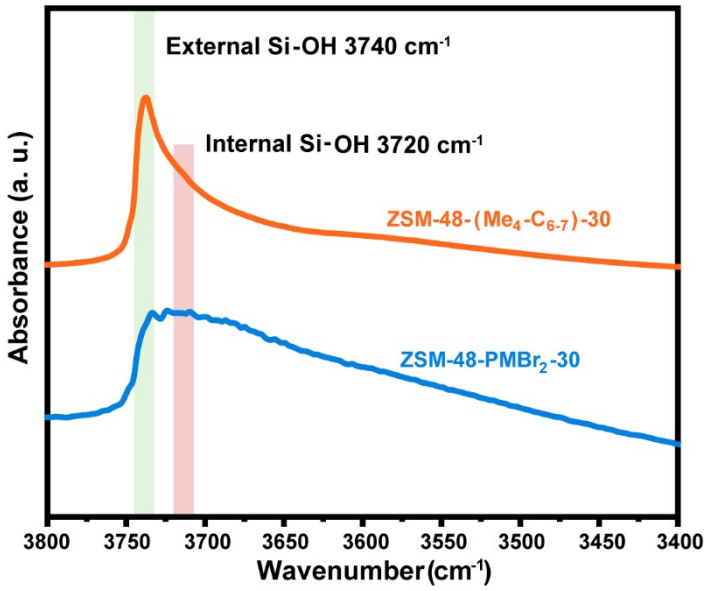

Figure S31. FT-IR spectra in the region of hydroxyl stretching vibration for HZSM-48-(Me_4-C_{6-7})-30 and HZSM-48-$PMBr_2$-30. The peaks at ca. 3740 cm^{-1} and 3720 cm^{-1} are assigned to terminal silanol locating on the external surface and internal silanol sites (defects), respectively[13]. HZSM-48-(Me_4-C_{6-7})-30 possesses a sharp band at ca. 3740 cm^{-1} and a rather weak shoulder band at 3720-3710 cm^{-1}, indicating the presence of a larger proportion of external surface silanol and traces of internal silanol. HZSM-48-$PMBr_2$-30 shows significant bands at 3720-3710 cm^{-1}, evidencing the existence of more intra-crystalline defects. The lowered internal silanol concentration originates from the bond-formation between neighboring domains, as explained in Fig. 4.

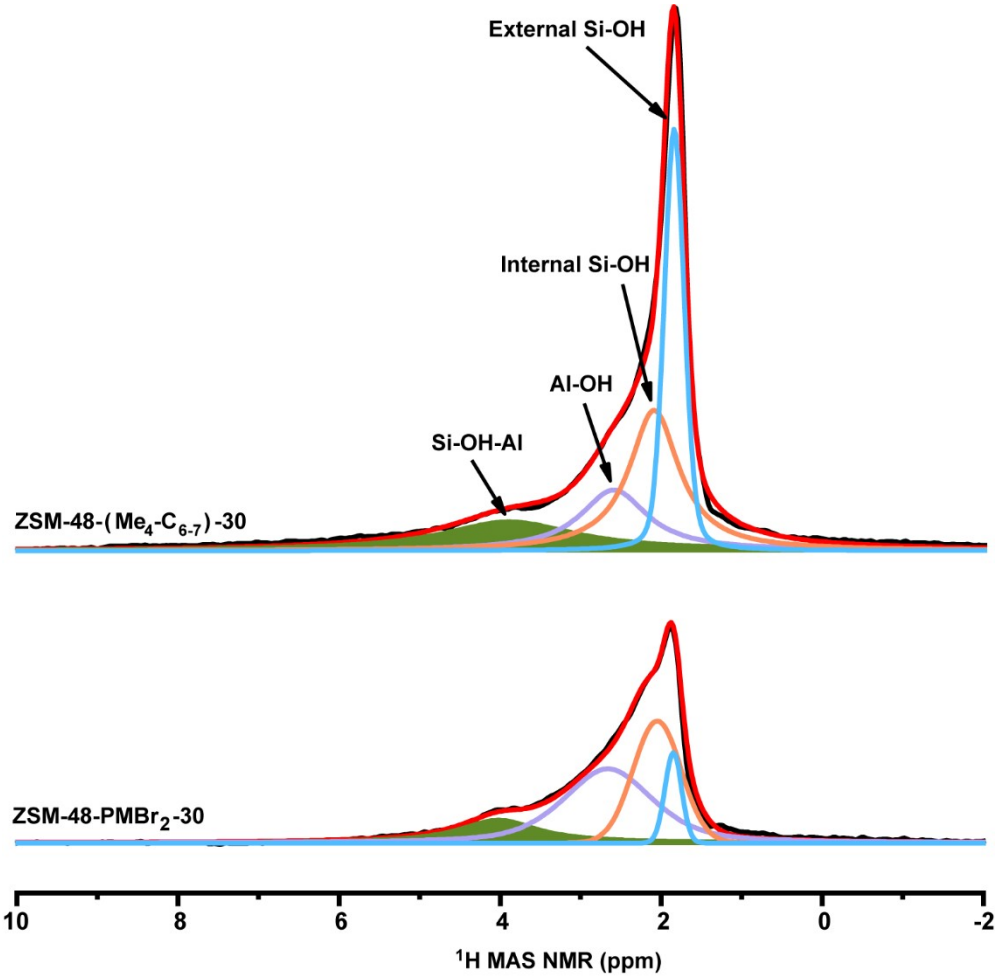

Figure S32. ^{1}H MAS NMR spectra for HZSM-48-(Me_4-$C_{6\text{-}7}$)-30 and HZSM-48-$PMBr_2$-30. The ^{1}H MAS NMR spectra confirmed that more external surface silanol groups (Si-OH, ~2.1 ppm) than internal ones (~1.8 ppm) in HZSM-48-(Me_4-$C_{6\text{-}7}$)-30.[14] Conversely, more internal defects are measurable in the control sample. As external defects often suggest termination of crystal growth, their large proportion in HZSM-48-(Me_4-$C_{6\text{-}7}$)-30 implies that the polycation Me_4-$C_{6\text{-}7}$ also serves as a growth modifier that interact strongly with the external surface of crystalline domains. Meanwhile, less determined internal defects are indicative of well-ordered structure and stronger acidity.

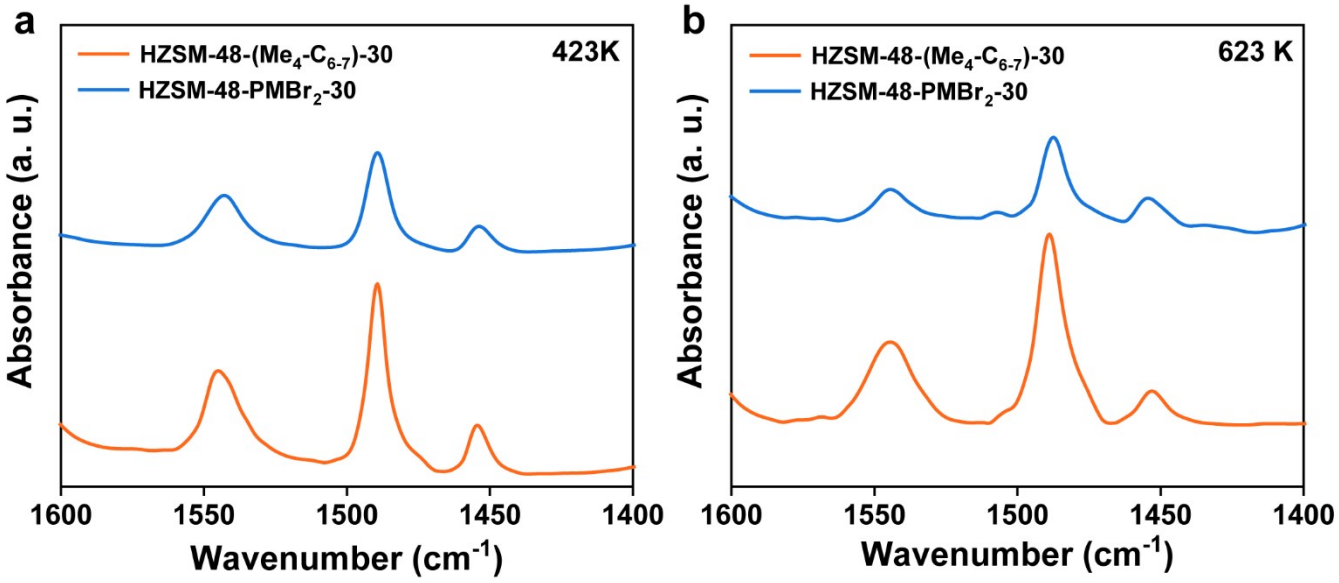

Figure S33. Py-IR of pyridine adsorbed on HZSM-48-(Me_4-C_{6-7})-30 and HZSM-48-$PMBr_2$-30 zeolites at 423 and 623 K.

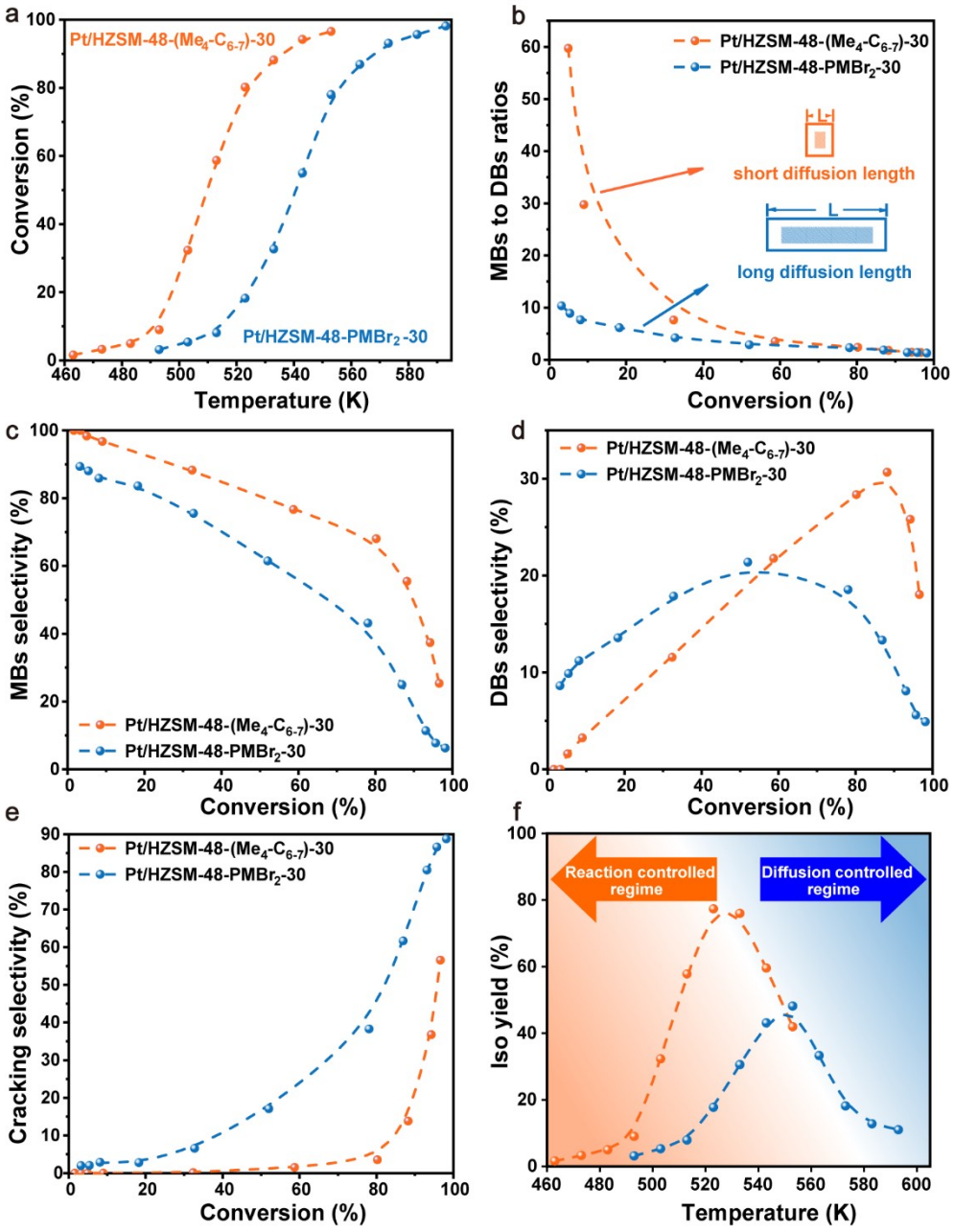

Figure S34. Catalytic performance of Pt/ZSM-48-(Me_4-C_{6-7})-30 and Pt/ZSM-48-$PMBr_2$-30 samples in *n*-dodecane hydroisomerization. Reactant conversion versus reaction temperature (463-553 K) (a), MBs/DBs ratio as a function of conversion (b), total MBs selectivity as function of conversions (c), total DBs selectivity as function of conversions (d) and total yield versus reaction temperature (f) in *n*-dodecane hydroisomerization. At low conversions, more MBs are determined in the products over Pt/HZSM-48-(Me_4-C_{6-7})-30 than Pt/HZSM-48-$PMBr_2$-30, because they are primary products and can easily escape from the shortened micropore channels in the former, whereas prolonged residence time in the channels of the latter has converted MBs into DBs. At elevated conversions, interconversion between MBs and DBs tend to minimize the difference, since the compositions reach identical, equilibrated values. According to previous investigations,[15, 16] isomer yield increases with temperature in the kinetic controlled, low temperature regime, while decreases after peaking and enters the diffusion controlled, high temperature regime. Here, the peak temperature for Pt/HZSM-48-(Me_4-C_{6-7})-30 has been decreased to 523 K for the stronger acidity. The increase in yield is associated with reduced residence time for DBs inside microchannels of Pt/HZSM-48-(Me_4-C_{6-7})-30, DBs are susceptible towards cracking with respect to MBs, and the unwanted DBs cracking can be exaggerated by prolonged residence time.[17-20]

3. Supplementary Tables

Table S1. The SDAs used and Si/Al ratio for the synthesis of ZSM-48 zeolites in literatures.

SDA	Gel composition	Crystallization conditions	Si/Al	Morphology	Ref.
HDA [a]	$405SiO_2$: Al_2O_3: $20.25Na_2O$: 607.5SDA	473 K, 480 h	202.5	Bundles of needles, 10-20 μm	21
Me_6-diquat-n [b]	$30SiO_2$: xAl_2O_3: $5Na_2O$:3SDA: $1200H_2O$	433 K, 168 h	30-∞	-	1
THP [c]	$110SiO_2$: $0.5Al_2O_3$: 0.43NaOH: 50SDA: $20H_2SO_4$: $5000H_2O$	443 K, 48 h	110	Fibrous rods or needles, 1-2 μm	22
TMACl [d]	$1SiO_2$: xAl_2O_3: $0.08Na_2O$:0.1SDA: $40H_2O$	443 K, 40-192 h	400-∞	Bundled needle, 2-4 μm	23
Diquaternary imidazole [e]	$100SiO_2$: xAl_2O_3: 10NaOH: 20SDA: $4000H_2O$	433 K, 96-480 h	300	-	24
MPMD [f]	$1.03SiO_2$: 8-10SDA:1-2HF:$10H_2O$	423 K, 120-480 h	∞	Aggregates of spatially oriented particles	25
$HMBr_2$ [g]	$75SiO_2$: $0.5Al_2O_3$: 3-$6Na_2O$: 2.5-10SDA: $3000H_2O$	463 K, 168 h	75	-	26
$HM(OH)_2$ [h]	$1SiO_2$: 0.25SDA: $5H_2O$	443 K, 504 h	∞	Needle-like crystals	27
$C_{22}N_6$ [i]	$100SiO_2$: $0.5Al_2O_3$: 26NaOH: 1.67SDA: $3000H_2O$	423 K, 72 h	110	Nanosponges	28
C_{12}TMABr [g]	$1SiO_2$:0.4NaOH:0.3SDA:20-$140H_2O$	433 K, 120-336 h	∞	Needle-like/rod-like crystals	29
C_{10}TMABr [k]	$1SiO_2$: $0.125Na_2O$: 0.025SDA: $17.5H_2O$	433 K, 72 h	∞	-	30
$C_{18\text{-}6\text{-}4}$ [l]	$100SiO_2$: $1Al_2O_3$: 7.5SDA: $28Na_2O$: $16H_2SO_4$: $5000H_2O$	423 K, 60 h	50	Nanosponges	31
N_2-p-N_2 [m]	$16SiO_2$: $0.4Al_2O_3$: 3.58NaOH: 1.2SDA: 128EtOH: $1143H_2O$	423 K, 120 h	106	Spherical, 300-400 nm	32
$N_{4\text{-phe}}$ [n]	$1SiO_2$:0.01-0.16Al_2O_3: 0.44NaOH: 0.05SDA: 8EtOH: $71H_2O$	413 K, 96-168 h	31-50	Platelet/nanorod	33
$BPT_{n\text{-}6\text{-}0}$ (n = 4, 6, 8, 10, 12) [o]	$30SiO_2$: 11.7NaOH: 1SDA: $2000H_2O$	413 K, 96 h	∞	Nanosheets	34
ATMA [p]	$30SiO_2$: $0.5Al_2O_3$: $4Na_2O$:9SDA: $1200H_2O$	433 K, 48 h	30	Needle-shaped crystals, 0.3-1.0 μm	35
HDA + TEABr [q]	$1SiO_2$: $0.004Al_2O_3$: 0.06NaOH: 0.45HDA: 0.05-0.2TEABr: $2000H_2O$	433 K, 72 h	125	Fibrotic nanorods, 200 nm	12
TBQA-1 [r]	$50SiO_2$: xAl_2O_3: 25NaOH: 4SDA: 200EtOH: $4000H_2O$	423 K, 120 h	100-500	Nanorods	36

[a]6-Hexylenediamine; [b]$(CH_3)_3N^+(CH_2)_nN^+(CH_3)_3$, n = 3, 5, 6, 8, 9, 10; [c]Pyrrolidine; [d]Tetramethylammonium chloride; [e]$(CH_3)_2CH(C_3H_3N_2)(CH_2)_n(C_3H_3N_2)CH(CH_3)_2$; [f]2-Methylpentamethylenediamine; [g]Hexamethonium bromide; [h]Hexamethonium; [i]$[C_{22}H_{45}\text{-}N^+(CH_3)_2\text{-}C_6H_{12}\text{-}N^+(CH_3)_2\text{-}CH_2\text{-}(C_6H_4)\text{-}CH_2\text{-}N^+(CH_3)_2\text{-}C_6H_{12}\text{-}N^+(CH_3)_2\text{-}CH_2\text{-}C_6H_4)\text{-}CH_2\text{-}N^+(CH_3)_2\text{-}C_6H_{12}\text{-}N^+(CH_3)_2\text{-}C_{22}H_{45}](Br^-)_2(Cl^-)_4$; [j]Dodecyltrimethyl ammonium bromide; [k]$CH_3(CH_2)_{10}N(CH_3)_3^+(Br^-)_2$; [l]$C_{18}H_{37}\text{–}N^+(CH_3)_2\text{–}C_6H_{12}\text{–}N^+(CH_3)_2\text{–}C_4H_9(Br^-)_2$; [m]$N^+(CH_3)_2\text{-}CH_2\text{-}(p\text{-}C_6H_4)\text{-}CH_2\text{-}N^+(CH_3)_2[Cl^-]_2$; [n]$C_{22}H_{45}N^+(CH_3)_2C_6H_{12}N^+(CH_3)_2CH_2C_6H_4CH_2N^+(CH_3)_2C_6H_{12}N^+(CH_3)_2C_{22}H_{45}(Br^-)_2(Cl^-)_2$; [o]$(C_6H_2)_3\text{-}(O\text{-}C_nH_{2n}\text{-}N^+(CH_3)_2\text{-}C_6H_{12}\text{-}N^+(CH_3)_2(Br^-))_6$; [p]Allyltrimethylammonium chloride; [q]Tetraethylammonium bromide; [r]$4,6\text{-}(CH_3O)_2\text{-}C_3N_3\text{-}N^+(CH_3)_2\text{-}C_6H_{12}\text{-}N^+(CH_3)_2\text{-}C_3N_3\text{-}4,6\text{-}(CH_3O)_2$

ZSM-48 is a typical unidimensional zeolite that exhibits excellent performance in *n*-paraffin hydroisomerization,[37] methanol to hydrocarbons,[38] *m*-xylene isomerization,[12] cracking of light naphtha,[39] the selective oxidation of cyclohexane[40] and catalytic oxidation of chlorophenol,[41] etc. In particular, it is the preferred industrial catalyst for hydroisomerization, a crucial petroleum refining process to boost low temperature flow properties of lubricant or diesel oil. Alkane hydroisomerization often use bifunctional catalysts comprising noble metal sites for (de)hydrogenation and acid sites for skeletal isomerization. The catalytic behaviors are dictated by acid and transport properties.[17, 42] Most of the ***MRE** zeolites are directed by soft small molecules, such as amines, diamines and diquaternary ammonium cations, and generally grow to bulk particles along 10-ring channel and suffer from diffusion limitation and less accessible acidity. The SDAs used for synthesis of ZSM-48 zeolites together with the Si/Al ratio and morphology of products are summarized from the literature survey, as listed in Table S1. Bottom-up protocols meet limited success since unidimensional zeolite habitually grow into rod-like crystals along the channel axis, which is regardless of the presence or absence of porogens. Until now, surfactants, such as $[C_{22}H_{45}\text{-}N^+(CH_3)_2\text{-}C_6H_{12}\text{-}N^+(CH_3)_2\text{-}CH_2\text{-}(C_6H_4)\text{-}CH_2\text{-}N^+(CH_3)_2\text{-}C_6H_{12}\text{-}N^+(CH_3)_2\text{-}CH_2\text{-}C_6H_4)\text{-}CH_2\text{-}N^+(CH_3)_2\text{-}C_6H_{12}\text{-}N^+(CH_3)_2\text{-}C_{22}H_{45}](Br^-)_2(Cl^-)_4$ ($C_{22}N_6$),[28] $(C_6H_2)_3\text{-}(O\text{-}C_nH_{2n}\text{-}N^+(CH_3)_2\text{-}C_6H_{12}\text{-}N^+(CH_3)_2(Br^-))_6$ ($BPT_{n\text{-}6\text{-}0}$)[34] and $C_{22}H_{45}N^+(CH_3)_2C_6H_{12}N^+(CH_3)_2CH_2C_6H_4CH_2N^+(CH_3)_2C_6H_{12}N^+(CH_3)_2C_{22}H_{45}](Br^-)_2(Cl^-)_2$ ($N_{4\text{-phe}}$)[33] are succeeded in the synthesis of hierarchical ZSM-48 zeolites. From a mass transfer viewpoint with regard to Thiele theorem, the reduction of diffusion path length along unidimensional channel direction is desirable for the enhancement of transport and catalytic performance, as have been demonstrated recently.[43] Considering the feature of ZSM-48 framework, we can speculate that main-chain type polymeric SDAs, of which the repeating segments are similar to hexamethonium ion (generally used as SDAs for ZSM-48 zeolite) but have a stronger complexation ability with aluminum species,[44] could conduct Al-rich hierarchical ZSM-48 with reduced channel-axis.

Table S2. Element analysis of chemical compositions for ZSM-48-(Me_4-C_{6-7}) of varied Si/Al ratios of starting gel , with the suffix indicating Si/Al ratios of the starting gels.

Sample	Si [a]	Al [a]	Si/Al [c]	Na [a]	C [b]	N [b]	H [b]
ZSM-48-(Me_4-C_{6-7})-20 [d]	38.00	1.84	19.91				
ZSM-48-(Me_4-C_{6-7})-30 [d]	33.40	1.20	26.84	0.61	8.39	1.11	2.18
ZSM-48-(Me_4-C_{6-7})-50 [d]	34.20	0.76	43.39	0.29	9.38	1.25	2.33
ZSM-48-(Me_4-C_{6-7})-100 [d]	32.6	0.41	76.67	0.12	9.70	1.27	2.52

[a]Determined by ICP-AES; [b]determined by elemental analysis; [c]calculated by the results of ICP-AES, element analysis and TGA; [d]the suffix 20, 30, 50 and 100 indicate Si/Al ratios of the starting gels.

Table S3. The isotropic chemical shifts, T-O-T bond angles, quadrupolar coupling constants and asymmetry parameters in ZSM-48-(Me_4-C_{6-7})-30 and ZSM-48-$PMBr_2$-30.

T-sites	ZSM-48-(Me_4-C_{6-7})-30				ZSM-48-$PMBr_2$-30			
	δ_{iso} (ppm) [a]	T-O-T bond angle [b]	C_Q (kHz) [b]	η [b]	δ_{iso} (ppm) [a]	T-O-T bond angle [b]	C_Q (kHz) [b]	η [b]
T1	-	-	-	-	65.03	133.94	3400	0.54
T2	58.29	147.42	3048	0.53	58.04	147.92	3051	0.52
T3	55.55	152.90	3261	0.52	55.30	153.40	3212	0.50
T4	60.91	142.18	2782	0.53	60.93	142.14	2980	0.49

[a]Calculated using the mean -Al-O-Si-bond angles for each T site from ZSM-48 and equation (1). [b]Extracted from analysis of 2D ^{27}Al 3Q MAS NMR spectrum in Fig. 3a, d, (δ_{iso}, isotropic chemical shift; C_Q, quadrupolar coupling constants; η, asymmetry parameters).

Table S4. Textural properties of ZSM-48-(Me_4-C_{6-7}) samples.

Sample	S_{BET} [m^2g^{-1}] [a]	S_{ext} [m^2g^{-1}] [b]	V_{total} [cm^3g^{-1}] [c]	V_{micro} [cm^3g^{-1}] [b]	V_{meso} [cm^3g^{-1}] [d]
ZSM-48-(Me_4-C_{6-7})-50	347	178	0.29	0.076	0.214
ZSM-48-(Me_4-C_{6-7})-100	331	158	0.27	0.078	0.192
ZSM-48-(Me_4-C_{6-7})-150	409	223	0.32	0.087	0.233
ZSM-48-(Me_4-C_{6-7})-200	344	159	0.28	0.087	0.193

[a]Calculated by the Brunauer-Emmett-Teller (BET) method. [b]Deduced by the *t*-plot method. [c]Calculated by the single point method at P/P_0 of 0.99. [d]$V_{meso} = V_{total}$-V_{micro}.

Table S5. Acidity ZSM-48-(Me_4-C_{6-7}) samples as determined by NH_3-IR measurements.

Samples	BAS (μmol g^{-1})		LAS (μmol g^{-1})	
	423 K	623 K	423 K	623 K
ZSM-48-(Me_4-C_{6-7})-50	318.2	88.2	18.5	11
ZSM-48-(Me_4-C_{6-7})-100	175.8	66.2	11.3	7.6
ZSM-48-(Me_4-C_{6-7})-150	114.7	41.3	9.1	6.4
ZSM-48-(Me_4-C_{6-7})-200	83.5	30.9	7.0	4.1

Table S6. Synthesis outcome from initial gel with molar composition: 30 SiO_2: x Al_2O_3: y NaOH: m SDA: n H_2O.

Entry #	x	y	m	n	Crystallization time (h)	Product
1	0.75	10	1.5	1200	216	***MRE**
2	0.5	10	1.5	1200	120	***MRE**
3	0.3	10	1.5	1200	120	***MRE**
4	0.15	10	1.5	1200	120	***MRE**
5	0.125	10	1.5	1200	144	***MRE**
6	0.1	10	1.5	1200	144	***MRE**
7	0.075	10	1.5	1200	144	***MRE**
8	0.05	10	1.5	1200	144	***MRE**
9	0	10	1.5	1200	144	***MRE**
10	0.5	12	1.5	1200	72	**MFI**
11	0.5	10.5	1.5	1200	72	**MFI**
12	0.5	9.3	1.5	1200	144	***MRE**
13	0.5	8.7	1.5	1200	168	***MRE**
14	0.5	8.1	1.5	1200	168	***MRE**
15	0.5	7.5	1.5	1200	216	***MRE**
16	0.5	6.9	1.5	1200	240	amorphous
17	0.5	10	1.5	600	240	amorphous
18	0.5	10	1.5	900	168	***MRE**
19	0.5	10	1.5	1500	144	***MRE**
20	0.5	10	1.5	1800	168	***MRE**
21	0.5	10	3	1200	120	***MRE**
22	0.5	10	4.5	1200	120	***MRE**

All syntheses were carried out under static condition at 423 K

Table S7. Solid state ^{27}Al MAS NMR dates of ZSM-48-(Me_4-C_{6-7})-30 in the course of crystallization.

Crystallization time (h)	^{27}Al chemical shift (ppm)	FWHM (ppm)
0	59.1	15.3
48	58.7	15.2
72	58.8	15.1
84	58.4	14.8
90	58.4	14.0
96	52.9	12.3
108	53.0	11.0
120	53.2	8.6

Table S8. Solid state ^{29}Si MAS NMR dates of ZSM-48-(Me_4-C_{6-7})-30 in the course of crystallization.

Crystallization time (h)	Amorphous Q^2 (ppm)	Amorphous Q^3 (ppm)	Q^3 $Si(OSi)_3OH$ (ppm)	Q^4 $Si(OSi)_3(OAl)$ (ppm)	Amorphous Q^4 (ppm)	Q^4 $Si(OSi)_4$ (ppm)
0	-91.8	-99.4	-	-	-109.9	-
48	-91.8	-99.6	-	-	-109.7	-
72	-91.8	-99.5	-	-	-109.7	-
84	-91.6	-99.5	-	-	-109.6	-
90	-91.7	-	-101.3	-	-	-112.3
96	-91.4	-	-101.5	-108.3	-	-113.2
108	-91.4	-	-101.6	-108.5	-	-113.2
120	-	-	-102.0	-108.5	-	-113.9

Table S9. Structural information from solid state ^{29}Si MAS NMR analysis on ZSM-48-(Me_4-C_{6-7})-30 in the course of crystallization.

Crystallization time (h)	Amorphous Q^2 (%)	Amorphous Q^3 (%)	Q^3 $Si(OSi)_3OH$ (%)	Amorphous $Q^4(1Al)$ (%)	Q^4 $Si(OSi)_3(OAl)$ (%)	Amorphous Q^4 (%)	Q^4 $Si(OSi)_4$ (%)
0	16.7	25.4	-	-	-	58.0	-
48	19.1	25.3	-	-	-	55.6	-
72	17.6	27.1	-	-	-	55.3	-
84	17.0	26.9	-	-	-	56.1	-
90	12.8	-	38.0	-	-	-	49.2
96	7.1	-	38.3	-	15.5	-	38.9
108	7.4	-	33.6	-	15.1	-	43.9
120	-	-	27.9	-	14.8	-	57.3

Table S10. Acidity and Pt dispersion of ZSM-48-30 samples as determined by NH_3-IR measurements and H_2 chemisorption.

Samples	BAS (μmol g^{-1}) [a]		LAS (μmol g^{-1}) [a]		BAS (μmol g^{-1}) [b]		LAS (μmol g^{-1}) [b]		Pt dispersion (%) (Pt_s/H^+) [c]
	423 K	623 K	423 K	623 K	423 K	623 K	423 K	623 K	
ZSM-48-(Me_4-C_{6-7})-30	557	114	557	21	58	43	15	9	30.9 (0.069)
ZSM-48-$PMBr_2$-30	474	46	474	19	36	16	12	5	16.8 (0.091)

[a]The number of Brønsted acid sites and Lewis acid sites were calculated from the NH_3-IR band area located at 1450 cm^{-1} and 1630 cm^{-1}, respectively[45].

[a]The number of Brønsted acid sites and Lewis acid sites were calculated from the Py-IR band area located at 1545 cm^{-1} and 1455 cm^{-1}, respectively[2].

[c]Determined by H_2 chemisorption after loading 0.5 wt. % of Pt. The Pt_s/H^+ ratios were estimated after normalizing surface Pt sites to BAS measured at 623 K.

Table S11. The product compositions at maximum isomer yield for *n*-dodecane hydroisomerization over samples.

Catalyst	Pt/HZSM-48-(Me_4-C_{6-7})-30	Pt/HZSM-48-$PMBr_2$-30
Temperature (K)	523	553
Conversion (%)	80.2	78.1
Total isomer yields (%)	77.4	48.2
2-C_{11} [a]	12.58	4.61
3-C_{11} [b]	12.86	8.86
4-C_{11} [c]	10.86	5.32
5/6-C_{11} [d]	19.86	14.89
3,6-C_{10} [e]	8.23	5.23
3,7-C_{10} [f]	6.21	4.47
3,8-C_{10} [g]	6.76	4.78
Cracking	2.86	29.89

[a] 2-methylundecane.
[b] 3-methylundecane.
[c] 4-methylundecane.
[d] 5-methylundecane or 6-methylundecane
[e] 3,6-dimethyldecane.
[f] 3,7-dimethyldecane.
[g] 3,8-dimethyldecane.

Table S12. Maximum isomer yields of zeolite catalyzed *n*-dodecane hydroisomerization in literature.

Catalysts	Reaction conditions	Isomer yield	Ref.
Pt/ZSM-48 (0.5 wt. % Pt)	H_2/*n*-C_{12} molar ratio = 15, WHSV = 2 $g_{n\text{-dodecane}}$ g_{cat}^{-1} h^{-1}, P = 0.1 MPa	60%	46
Pt/ZSM-48 (0.5 wt. % Pt)	H_2/*n*-C_{12} molar ratio = 6058, LHSV = 2 $m^3_{n\text{-dodecane}}$ $m^3_{cat}{}^{-1}$ h^{-1}, P = 0.1 MPa	17.7%	47
Pt/ZSM-48 (alkali treated, 0.5 wt. % Pt)	H_2/*n*-C_{12} molar ratio = 6058, LHSV = 2 $m^3_{n\text{-dodecane}}$ $m^3_{cat}{}^{-1}$ h^{-1}, P = 0.1 MPa	27.7%	
Pt/ZSM-48 (0.5 wt. % Pt)	H_2/*n*-C_{12} molar ratio = 20, WHSV = 1.5 $g_{n\text{-dodecane}}$ g_{cat}^{-1} h^{-1}, P = 3 MPa	63%	48
Ni/ZSM-48 (conventional, 1 wt. % Ni)	H_2/*n*-C_{12} molar ratio = 20, WHSV = 1.5 $g_{n\text{-dodecane}}$ g_{cat}^{-1} h^{-1}, P = 3 MPa	49%	
Ni/ZSM-48 (nanosponge, 1 wt. % Ni)	H_2/*n*-C_{12} molar ratio = 20, WHSV = 1.5 $g_{n\text{-dodecane}}$ g_{cat}^{-1} h^{-1}, P = 3 MPa	73%	
Pt/GaZSM-48 (0.5 wt. % Pt, Al/Ga = 1)	H_2/*n*-C_{12} molar ratio = 1200, LHSV = 2 $m^3_{n\text{-dodecane}}$ $m^3_{cat}{}^{-1}$ h^{-1}, P = 2 MPa	76%	49
Pt/FeZSM-48 (0.5 wt. % Pt, Al/Fe = 5)	H_2/*n*-C_{12} molar ratio = 1200, LHSV = 2 $m^3_{n\text{-dodecane}}$ $m^3_{cat}{}^{-1}$ h^{-1}, P = 2 MPa	58.9%	50
Pt/ZSM-48 (0.5 wt. % Pt)	H_2/*n*-C_{12} molar ratio = 490, WHSV = 0.75 $g_{n\text{-dodecane}}$ g_{cat}^{-1} h^{-1}, P = 0.1 MPa	77.4%	This work

4. Supplementary Video

Video S1. Electron tomography of ZSM-48-(Me_4-C_{6-7})-30.

5. References

1. S. H. Lee, C. H. Shin, D. K. Yang, S. D. Ahn, I. S. Nam and S. B. Hong, *Microporous Mesoporous Mater.*, 2004, **68**, 97-104.
2. C. A. Emeis, *J. Catal.*, 1993, **141**, 347-354.
3. T. Barzetti, E. Selli, D. Moscotti and L. Forni, *J. Chem. Soc., Faraday trans.*, 1996, **92**, 1401-1407.
4. R. Lifshitz and H. Diamant, *Philos Mag.*, 2007, **87**, 3021-3030.
5. E. Lippmaa, A. Samoson and M. Mägi, *J. Am. Chem. Soc.*, 1986, **108**, 1730-1735.
6. A. Samoson and E. Lippmaa, *Chem. Phys. Lett.*, 1987, **134**, 589-592.
7. S. Wang, B. He, R. Tian, C. Sun, R. Dai, X. Li, X. Wu, X. An and X. Xie, *J. Colloid Interface Sci.*, 2018, **527**, 339-345.
8. S. Mintova, M. Jaber and V. Valtchev, *Chem. Soc. Rev.*, 2015, **44**, 7207-7233.
9. S. Kim, G. Park, M. H. Woo, G. Kwak and S. K. Kim, *ACS Catal.*, 2019, **9**, 2880-2892.
10. P. Lu, S. Ghosh, M. D. de Mello, H. S. Kamaluddin, X. Li, G. Kumar, X. Duan, M. Abeykoon, J. A. Boscoboinik, L. Qi, H. Dai, T. Luo, S. Al-Thabaiti, K. Narasimharao, Z. Khan, J. D. Rimer, A. T. Bell, P. Dauenhauer, K. A. Mkhoyan and M. Tsapatsis, *Angew. Chem. Int. Ed.*, 2021, **60**, 19214-19221.
11. J. Grand, H. Awala and S. Mintova, *CrystEngComm*, 2016, **18**, 650-664.
12. W. Liu, J. Li, Z. Liu, Z. Yang, X. Liu, X. Tan, L. Xu, X. Li and X. Zhu, *ACS Appl. Mater. Interfaces*, 2021, **13**, 31756-31765.
13. I. C. Medeiros-Costa, E. Dib, N. Nesterenko, J. P. Dath, J. P. Gilson and S. Mintova, *Chem. Soc. Rev.*, 2021, **50**, 11156-11179.
14. Z. Wang, L. Wang, Z. Zhou, Y. Zhang, H. Li, C. Stampfl, C. Liang and J. Huang, *J. Phys. Chem. C*, 2017, **121**, 15248-15255.
15. T. Yue, W. i. Liu, L. Li, X. Zhao, K. Zhu, X. Zhou and W. Yang, *J. Catal.*, 2018, **364**, 308-327.
16. D. Jin, G. Ye, J. Zheng, W. Yang, K. Zhu, M. O. Coppens and X. Zhou, *ACS Catal.*, 2017, **7**, 5887-5902.
17. G. Noh, Z. Shi, S. I. Zones and E. Iglesia, *J. Catal.*, 2018, **368**, 389-410.
18. G. Noh, S. I. Zones and E. Iglesia, *J. Catal.*, 2019, **377**, 255-270.
19. Z. Qin, S. Zeng, G. Melinte, T. Bučko, M. Badawi, Y. Shen, J. P. Gilson, O. Ersen, Y. Wei, Z. Liu, X. Liu, Z. Yan, S. Xu, V. Valtchev and S. Mintova, *Adv. Sci.*, 2021, **8**, 2100001.
20. G. Noh, S. I. Zones and E. Iglesia, *J. Phys. Chem. C*, 2018, **122**, 25475-25497.
21. R. Li, W. Fan, J. Ma, B. Fan and J. Cao, *Zeolites*, 1995, **15**, 73-76.
22. P. Meriaudeau, V. A. Tuan, V. T. Nghiem, G. Sapaly and C. Naccache, *J. Catal.*, 1999, **185**, 435-444.
23. K. Suzuki and T. Hayakawa, *Microporous Mesoporous Mater.*, 2005, **77**, 131-137.
24. S. I. Zones and A. W. Burton, *J. Mater. Chem.* , 2005, **15**, 4215-4223.
25. S. Ferdov, Z. Lin and R. A. S. Ferreira, *Chem. Lett.*, 2008, **37**, 100-101.
26. G. Giordano, J. B. Nagy and E. G. Derouane, *J. Mol. Catal. A: Chem.*, 2009, **305**, 34-39.
27. X. Liu, U. Ravon and A. Tuel, *Microporous Mesoporous Mater.*, 2012, **156**, 257-261.
28. W. Kim, J. C. Kim, J. Kim, Y. Seo and R. Ryoo, *ACS Catal.*, 2013, **3**, 192-195.
29. T. Moteki, S. H. Keoh, T. Ohmura, K. Iyoki, T. Wakihara and T. Okubo, *J. Ceram. Soc. Jpn.*, 2013, **121**, 575-577.
30. T. Moteki, S. H. Keoh and T. Okubo, *Chem. Comm.* , 2014, **50**, 1330-1333.
31. S. Lee, C. Jo and R. Ryoo, *J. Mater. Chem. A*, 2017, **5**, 11086-11093.
32. K. Zhang, C. Li, Z. Liu, M. Wang, X. Yan and H. Xi, *Chem. - Asian J.*, 2017, **12**, 2711-2719.
33. A. Astafan, M. A. Benghalem, L. Michelin, S. Rigolet, J. Patarin, L. Pinard and T. J. Daou, *New J. Chem.*, 2018, **42**, 4457-4464.
34. Y. Zhang, Y. Ma and S. Che, *Chem. Mater.*, 2018, **30**, 1839-1843.

35. M. Zhai, H. Ding, S. Zeng, J. Jiang, S. Xu, X. Li, K. Zhu and X. Zhou, *Ind. Eng. Chem. Res.*, 2020, **59**, 11139-11148.
36. R. Wang, Z. Peng, P. Wu, H. Sun, Y. Zhang, F. Subhan, H. Yin, Y. Wang and Z. Yan, *Inorg. Chem. Front.*, 2022, **9**, 2016-2022.
37. J. Meng, D. Bai, P. Zeyaodong, C. Li, X. Chen and C. Liang, *Microporous Mesoporous Mater.*, 2022, **330**, 111637.
38. J. Zhang, Z. Huang, L. Xu, X. Zhang, X. Zhang, Y. Yuan and L. Xu, *Catal. Sci. Technol.*, 2019, **9**, 2132-2143.
39. M. H. M. Ahmed, T. Masuda and O. Muraza, *Fuel*, 2019, **258**, 116034.
40. R. S. Wang, Z. H. Peng, P. P. Wu, H. M. Sun, Y. Zhang, F. Subhan, H. L. Yin, Y. H. Wang and Z. F. Yan, *Inorg. Chem. Front.*, 2022, **9**, 2016-2022.
41. K. S. Lin and H. P. Wang, *J. Phys. Chem. B*, 2001, **105**, 4956-4960.
42. R. Gounder and E. Iglesia, *J. Catal.*, 2011, **277**, 36-45.
43. Y. Zheng, H. Ding, E. Xing, J. Zhou, Y. Luo, J. Liu and K. Zhu, *Catal. Today*, 2022, **405**, 30-46.
44. C. Lei, Z. Dong, C. Martnez, J. M. Triguero, W. Chen, Q. Wu, X. Meng, A. N. Parvulescu, T. D. Baerdemaeker, U. Muller, A. Zheng, Y. Ma, W. Zhang, T. Yokoi, B. Marler, D. E. D. Vos, U. Kolb, A. Corma and F. S. Xiao, *Angew. Chem. Int. Ed.*, 2020, **59**, 15649-15655.
45. T. Barzetti, E. Selli, D. Moscotti and L. Forni, *J. Chem. Soc., Faraday Trans.*, 1996, **92**, 1401-1407.
46. S. Yun, E. Lee, Y.-K. Park, S.-Y. Jeong, J. Han, B. Jeong and J.-K. Jeon, *Res. Chem. Intermed.*, 2011, **37**, 1215-1223.
47. Y. Wang, W. Liu, W. Zhang, J. Sun, S. Li, J. Zheng, B. Fan and R. Li, *Catal. Lett.*, 2021, **151**, 3492-3500.
48. J. Kim, S. W. Han, J.-C. Kim and R. Ryoo, *ACS Catal.*, 2018, **8**, 10545-10554.
49. W. Zhang, H. Zhang, M. Ma, S. Wang, J. Xiang, Y. Wang, W. Dai, B. Fan, J. Zheng and R. Li, *React. Chem. Eng.*, 2023, **8**, 2481-2490.
50. J. N. Xiang, W. Zhang, H. P. Zhang, S. Z. Wang, M. X. Ma, Y. T. Wang, Y. Wang, W. J. Dai, B. B. Fan, J. J. Zheng, J. H. Ma and R. F. Li, *Solid State Sci.*, 2023, **142**, 107250.